Fragmentation inside PTR-based mass spectrometers limits the detection of ROOR and ROOH peroxides

Haiyan Li[1,2,†], Thomas Golin Almeida[3,†], Yuanyuan Luo[2], Jian Zhao[2], Brett B. Palm[4], Christopher D. Daub[3], Wei Huang[2], Claudia Mohr[5], Jordan E. Krechmer[6], Theo Kurtén[3], Mikael Ehn[2]

[1]School of Civil and Environmental Engineering, Harbin Institute of Technology, Shenzhen, 518055
[2]Institute for Atmospheric and Earth System Research / Physics, Faculty of Science, University of Helsinki, Helsinki, 00014, Finland
[3]Department of Chemistry, University of Helsinki, Helsinki, 00014, Finland
[4]Department of Atmospheric Science, University of Washington Seattle, Washington, WA, 98195, USA
[5]Department of Environmental Science, Stockholm University, 11418, Stockholm, Sweden
[6]Aerodyne Research, Inc., Billerica, MA, 01821, USA
†These authors contributed equally to this work.

Correspondence to: Haiyan Li (lihaiyan2021@hit.edu.cn), Mikael Ehn (mikael.ehn@helsinki.fi), Theo Kurtén (theo.kurten@helsinki.fi)

Abstract. Proton-transfer-reaction (PTR) is a commonly applied ionization technique for mass spectrometers, where hydronium ions (H_3O^+) transfer a proton to analytes with higher proton affinities than the water molecule. This method has most commonly been used to quantify volatile hydrocarbons, but later generation PTR-instruments have been designed for better throughput of less volatile species, allowing detection of more functionalized molecules as well. For example, the recently developed Vocus PTR time-of-flight mass spectrometer (PTR-TOF) has been shown to agree well with an iodide adduct based chemical ionization mass spectrometer (CIMS) for products with 3-5 O-atoms from oxidation of monoterpenes ($C_{10}H_{16}$). However, while several different types of CIMS instruments (including those using iodide) detect abundant signals also at “dimeric” species, believed to be primarily ROOR peroxides, no such signals have been observed in the Vocus PTR, even though these compounds fulfil the condition of having higher proton affinity than water.

More traditional PTR instruments have been limited to volatile molecules as the inlets have not been designed for transmission of easily condensable species. Some newer instruments, like the Vocus PTR, have overcome this limitation, but are still not able to detect the full range of functionalized products, suggesting that other limitations need to be considered. One such limitation, well-documented in PTR literature, is the tendency of protonation to lead to fragmentation of some analytes. In this work, we evaluate the potential for PTR to detect dimers and the most oxygenated compounds, as these have been shown to be crucial for forming atmospheric aerosol particles. We studied the detection of dimers using a Vocus PTR-TOF in laboratory experiments as well as through quantum chemical calculations. Only noisy signals of potential dimers were observed during experiments on the ozonolysis of the monoterpene α-pinene, while a few small signals of dimeric compounds were detected during the ozonolysis of cyclohexene. During the latter experiments, we also tested varying the pressures and electric fields in the ionization region of the Vocus PTR-TOF, finding that only small improvements were possible in the relative dimer contributions. Calculations for model ROOR and ROOH systems showed that most of these peroxides should fragment partially following protonation. With inclusion of additional energy from the ion-molecule collisions driven by the electric fields in the ionization source, computational results suggest substantial or nearly complete fragmentation of dimers. Our study thus suggests that while the improved versions of PTR-based mass spectrometers are very powerful tools for measuring hydrocarbons and their moderately oxidized products, other types of CIMS are likely more suitable for the detection of ROOR and ROOH species.

1 Introduction

Volatile organic compounds (VOCs) are emitted into the atmosphere from a variety of sources, both biogenic (Kesselmeier and Staudt, 1999;Sindelarova et al., 2014) and anthropogenic (Friedrich and Obermeier, 1999;Theloke and Friedrich, 2007;Huang et al., 2011). The major atmospheric loss process of these VOCs is oxidation, and the oxidation process can contribute to the formation of harmful pollutants such as tropospheric ozone (Carter, 1994;Ying and Krishnan, 2010) and organic particulate matter (Chen et al., 2011;Ehn et al., 2014). The ability of a specific VOC to produce organic aerosol depends on how efficiently the VOC is converted to low-volatile species during the oxidation process (Donahue et al., 2012). Oligomerization and oxygenation tend to lower the volatility, making the products more likely to condense into the particulate phase, while fragmentation typically has the opposite effect by increasing the volatilities of the products (Jimenez et al., 2009). As atmospheric aerosol particles greatly affect Earth's radiative balance (Charlson et al., 1992;Rap et al., 2013), the relative branching ratios between these three pathways, and the oxidation process in general, is of great importance.

In the last decade, online chemical ionization mass spectrometers (CIMS) have become increasingly applied in atmospheric studies of VOC oxidation (Bertram et al., 2011;Jokinen et al., 2012;Lee et al., 2014b;Krechmer et al., 2018;Lopez-Hilfiker et al., 2019). Their high sensitivity and high time resolution have provided detailed information on a vast number of oxidation products, both in gas and aerosol phase, leading to a suite of new insights and breakthroughs (Ehn et al., 2014;Bianchi et al., 2019;Mohr et al., 2019). In some cases, nearly full mass closure has been achieved between precursors and products (Hansel et al., 2018;Isaacman-VanWertz et al., 2018). Ultimately, the type of CIMS being deployed, defined primarily by the choice of reagent ion and the inlet design, determine the selectivity of the instrument (Riva et al., 2019). Some instruments are mainly selective towards the most oxygenated species, like the Chemical Ionization Atmospheric Pressure interface Time-of-Flight mass spectrometers (CI-APi-TOF) using NO_3^- as the reagent ion (Hyttinen et al., 2015;Yan et al., 2016), while others primarily detect moderately oxidized products, like the iodide (I^-)-CIMS (Lee et al., 2014a). Many of these commonly used selective ion-molecule reactions have been solidly supported and explained through computational studies of clustering strengths between reagent ions and different types of organic compounds (Kupiainen-Määttä et al., 2013;Iyer et al., 2017;Hyttinen et al., 2018). For the detection of precursor VOCs, the most typical CIMS type used has been proton-transfer-reaction (PTR) mass spectrometry, which is based on the transfer of a proton from a hydronium ion (H_3O^+) to an analyte with higher proton affinity (Yuan et al., 2017). Earlier versions of PTR instruments have been designed to measure only very volatile compounds, but more recent designs like the PTR3 (Breitenlechner et al., 2017) and the Vocus PTR (Krechmer et al., 2018) have shown their ability to detect also less volatile oxidation products in addition to the precursor VOC.

Good agreement between different CIMS types has been seen for specific compound groups. As shown recently e.g. in a CIMS intercomparison study (Riva et al., 2019), moderately oxidized monomeric products agreed well between an iodide CIMS and a Vocus PTR in the mass range of < 300 Th. The compounds above ~300 Th likely contain organic hydroperoxides, ROOH, or organic peroxides, ROOR. The former are mainly formed from the reaction of organic peroxy radicals (RO_2) with HO_2 or in the process of autoxidation(Crounse et al., 2013), while the latter form from cross reactions of RO_2 (Schervish and Donahue, 2020;Tomaz et al., 2021). The CI-APi-TOF instruments using either NO_3^- or $C_4H_{12}N^+$ (butylamine) as reagent ions agreed well for highly oxygenated accretion products, which are believed to be primarily ROOR dimers. ~~, while highly oxygenated accretion products agreed well between CI-APi-TOF instruments using either NO_3^- or $C_4H_{12}N^+$ (butylamine) as reagent ions. These accretion products are believed to be primarily peroxide dimers, ROOR, formed from cross reactions of peroxy radicals, RO_2~~ (Schervish and Donahue, 2020;Tomaz et al., 2021). Similarly, aminium CI-APi-TOF and the ammonium adduct PTR3 matched well over a wide range of oxidation products under very clean conditions (Berndt et al., 2018b). However, to our knowledge, with the exception of the PTR3, temporal agreement between any CIMS instruments (including the iodide CIMS and the Vocus PTR) and a nitrate CI-APi-TOF has never been shown for the most highly oxygenated products. Additionally, no accretion products, i.e. "dimers" (Berndt et al., 2018b;Valiev et al., 2019), have been reported for any other PTR instruments than the PTR3 (where ionization can also take place as ligand switching from protonated water clusters) (Breitenlechner et al., 2017), although the other chemical reagent ions regularly detected them. As one of the very few types of commonly used CIMS which has also been optimized for measurements of hydrocarbon VOC, these apparent limitations are disappointing as PTR instruments like the Vocus PTR could otherwise provide a uniquely broad range of observations of both precursors and products. One possible reason for this limitation, also speculated by Riva et al. (2019) regarding the lack of detected dimer species by a Vocus PTR, is that protonation leads to fragmentation, a process which is known to be common for different types of hydrocarbons in PTR instruments (Tani et al., 2003;Aprea et al., 2007;Gueneron et al., 2015;Pagonis et al., 2019)..

In this work, we aimed to characterize the ability of a PTR mass spectrometer to detect ROOR and ROOH species, both experimentally and computationally. We performed experiments using a Vocus PTR-TOF to measure oxidation products from different precursors, and varied the settings under which the ionization took place, to identify parameters that influence the detection of dimeric compounds. Quantum chemical calculations were performed for both ROOR and ROOH systems to estimate to what extent, and through which channels, the protonation and subsequent ion transport could lead to fragmentation before detection.

2 Materials and methods

2.1 Experimental methods

To test the ability of PTR mass spectrometry to detect ROOR species, we deployed a Vocus PTR-TOF in chamber experiments of VOC oxidation known to produce a wide range of products with different functionalities. We acknowledge that the Vocus PTR is only one of many PTR designs, and while the basic principle of proton transfer from hydronium ions is common for all instruments, differences in design and operation may impact the general applicability of our experimental findings. In the chamber experiments, ozone was reacted with either α-pinene, a monoterpene and one of the most abundantly emitted VOCs globally (Guenther et al., 2012), or cyclohexene, a commonly used surrogate for monoterpenes. These systems were chosen because they are known to produce a large number of different dimer species (Berndt et al., 2018a;Rissanen et al., 2014;Hansel et al., 2018).

The laboratory experiment was conducted in a 2 m^3 atmospheric simulation Teflon FEP (fluorinated ethylene propylene) chamber at the University of Helsinki. More details about the chamber have been presented by Riva et al. (2019) and Peräkylä et al. (2020). The chamber was operated under steady-state conditions with a constant flow of reactants and oxidants continuously added to the chamber. The chamber was maintained at a slight overpressure, and the average residence time was ~45 min. The majority of the chamber flow was sampled by a variety of instruments, including the Vocus PTR-TOF, with the rest flushed into an exhaust line. We performed the α-pinene/cyclohexene ozonolysis experiments in the absence of an OH scavenger at room temperature (27 ± 2 °C) and under dry conditions (RH < 1%). The dry air was purified with a clean air generator (AADCO model 737-14, Ohio, USA) and injected into the chamber along with the gaseous reactants. Ozone was generated by injecting purified air through an ozone generator (Dasibi 1008-PC). α-pinene or cyclohexene addition into the chamber was controlled by a heated syringe pump. Ozone concentrations in the chamber were monitored by a UV photometric analyzer (Model 49P, Thermo-Environmental) during cyclohexene ozonolysis, but the analyser was not available during α-pinene ozonolysis experiments.

The Vocus PTR-TOF utilizes a low-pressure discharge reagent-ion source to produce H_3O^+ reagent ions, which are subsequently mixed with sample air in a focusing ion-molecule reactor (FIMR) (Krechmer et al., 2018). The FIMR consists of a resistive glass tube with four quadrupole rods mounted radially on the outside. The glass tube improves measurement delay times and transmission by eliminating any metal surfaces for gaseous molecules or ions to adsorb to. The ions are transported through the 10 cm-long FIMR using a DC (direct current) electric field, with a typical potential gradient of 450-650 V (500 V in these experiments as default) and a variable quadrupole RF (radio frequency) field applied transversely to focus ions along the central axis. The pressure in the FIMR was kept at 1.4 mbar, except for experiments where the influence of pressure on the mass spectra was probed. In this study, sample air with a flow rate of 4.5 L min^{-1} was drawn through 1 m long PTFE (polytetrafluoroethylene) tubing (6 mm o.d., 4 mm i.d.), out of which around 0.1 L min^{-1} went into the FIMR and the remainder was directed to the exhaust. The Vocus ionization source was operated with a 15 sccm flow of pure water vapor.

For a molecule R with higher proton affinity than H_2O, ionization can occur via proton transfer from H_3O^+ to produce the product ion ($[RH]^+$)

$$R + H_3O^+ \rightarrow [RH]^+ + H_2O \qquad \text{(Rp)}$$

The PTR technique is considered a soft ionization method when compared to, e.g., electron impact ionization. However, the $[RH]^+$ ions produced from the above reaction can still undergo fragmentation in the reactor due to the added energy from the exothermic protonation reaction as well as collisions (Gueneron et al., 2015;Tani et al., 2003;Tani et al., 2004). While higher collision energy reduces clustering of the reagent and product ions with water, it can also promote fragmentation of the protonated ions. The fragmentation inside the PTR strongly depends on the parameter E/N, the ratio of the guiding electric field to the number density of the gas in the PTR drift tube. An increase in E/N results in more energetic collisions and thus an increased degree of fragmentation (Gueneron et al., 2015).

2.2 Computational methods

To investigate fragmentation patterns in a less instrument-specific manner, quantum chemical methods were used to calculate the energetics of gas-phase fragmentation pathways available to a selection of protonated model ROOR and ROOH compounds. In an elementary reaction, reactants and products are connected by a transition state, defined as the point of highest potential energy in the reaction coordinate. The transition state represents a barrier that must be surpassed for the reaction to occur, and knowledge of its energy relative to the reactant (i.e. the barrier height) allows one to predict the thermal rate of the reaction. However, the studied reactions happen in low pressures and the preceding protonation step is exothermic. Collisions with bath gas molecules may be too rare to rapidly dissipate the energy accumulated during protonation, and a portion of the peroxide molecules may fragment at non-thermal rates. Thus, appropriate analysis of fragmentation in this case requires treatment of collisional energy transfer and energy-specific microcanonical rates, which are included in master equation solvers. Calculation of the Potential Energy Surface (PES), i.e. the energy of each reactant, intermediate, transition state and product involved in a reaction mechanism, was employed to predict how fast a series of model protonated peroxides fragment and which would be their product yields.

The model ROOR systems studied were: methyl peroxide (MeOOMe), ethyl peroxide (EtOOEt), isopropyl peroxide (iPrOOiPr), hydroxyethyl methyl peroxide (HOEtOOMe), oxoethyl methyl peroxide (O=EtOOMe) and acetyl peroxide (AcOOAc); and the model ROOH systems were: methyl hydroperoxide (MeOOH), ethyl hydroperoxide (EtOOH), isopropyl hydroperoxide (iPrOOH), tert-butyl hydroperoxide (tButOOH), hydroxyethyl hydroperoxide (HOEtOOH), oxoethyl hydroperoxide (O=EtOOH), peracetic acid (AcOOH) and performic acid (OCHOOH). In addition, selected ROOR and ROOH systems derived from cyclohexene oxidation initiated by OH radical and ozone were also studied (Figure 1). These compounds are 2,2'-peroxy bis(hexanedial) (**A**), 2-hydroperoxyhexanedial (**B**), 2,2'-peroxy bis(cyclohexanol) (**C**) and 2-hydroperoxycyclohexanol (**D**).

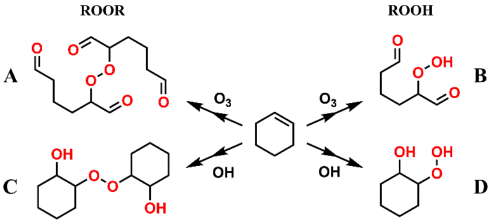

Figure 1. Investigated ROOR and ROOH species derived from oxidation of cyclohexene by OH radical and O_3.

Initial systematic conformer search was performed for each species involved in the studied reactions with the Merck Molecular Force Field (MMFF) method (Halgren, 1999)~~(Halgren, 1999)~~ implemented in~~ Spartan '18~~ Spartan'18 (2018)~~ (2018)~~. All conformers were then optimized at the B3LYP/6-311++G** level of theory (Becke, 1993;Lee et al., 1988)~~ (Becke, 1993;Lee et al., 1988)~~, and the ones yielding the lowest electronic energies (within 2 kcal ~~·~~mol^{-1}) were reoptimized at the ωB97XD/aug-cc-pVTZ level (Chai and Head-Gordon, 2008;Kendall et al., 1992)~~ (Chai and Head-Gordon, 2008;Kendall et al., 1992)~~, using Gaussian'16 RevC.01 (Frisch et al., 2016)~~ (Frisch et al., 2016)~~. Subsequent frequency calculations provided vibrational frequencies and rotational constants, and served to ensure that all optimized geometries correspond to stationary points in the PES. Conformer geometries with similar electronic energy and electric dipole (difference less than 10^{-5} Hartree and 0.015 Debye respectively) were identified as duplicates and removed (Møller et al., 2016)~~ (Møller et al., 2016)~~. Initial guesses for some of the transition state (TS) geometries of the simplest systems, MeOOMe and MeOOH, were taken from a study published by Schalley et al. (1997). Transition states for other steps were found by doing relaxed scans over critical bond lengths or angles, and some were found during the geometry optimization of conformers of unrelated transition states. Intrinsic Reaction Coordinate (IRC) calculations were done for each transition state, at the B3LYP/6-311++G** level of theory, in order to check if they correctly connect to the assumed reactant and product minima. Finally, more accurate electronic energies were obtained for the lowest energy conformer of each species, by performing single point RHF-RCCSD(T)-F12a/VDZ-F12 calculations (Knizia et al., 2009)~~ (Knizia et al., 2009)~~, with the Molpro 2019.2 software (Werner et al., 2012)~~(Werner et al., 2012)~~.

Once the PES of each model ROOR and ROOH system was obtained, the time-dependent species distribution profile was estimated with MESMER (Master Equation Solver for Multi-Energy Well Reactions) version 5.2 (Glowacki et al., 2012) ~~(Glowacki et al., 2012)~~. Rice-Ramsperger-Kassel-Marcus (RRKM) theory was used to treat isomerization reaction steps and the reverse Inverse Laplace Transformation (ILT) method was used for irreversible dissociation steps. The initial charged species (RH^+) were modelled as having emerged from a barrierless dissociation reaction, $A(E_{ex}) \rightarrow RH^+ + H_2O$, where E_{ex} is the excess energy in reactant A, which was assumed to be equal to the zero-point corrected energy of reaction Rp (ΔE_{zp}). The exponential down model was employed to treat collisional energy transfer. Lennard-Jones parameters and $\langle \Delta E_{down} \rangle$ values used were fitted to molecular dynamics (MD) simulation results for thermalization rates of three model $(ROOR)H^+$

Formatted: Superscript

species. While mathematical methods for obtaining these parameters used in master equation methodologies have been developed (Barker, 2009;Barker and Weston, 2010;Jasper et al., 2014), the complexity of these approaches means that in practice, many researchers use some method to empirically fit the thermal transfer process. In this work, we introduce a simplified method to reliably fit the thermal equilibration profile. In brief, we use classical MD to directly measure the collision driven thermal decay rate, followed by empirically fitting the Lennard-Jones parameters in the stochastic gas collision model used within MESMER to match the collision frequency and the thermal decay measured by MD. -Further details on the methods are found in the Supplementary Information.

3 Results and discussion

3.1 Oxidation products from α-pinene ozonolysis

Figure 2a shows the average mass spectra of Vocus PTR-TOF measurements during α-pinene ozonolysis ([α-pinene] = 82.4 ± 148.8 ppb), covering both α-pinene and α-pinene oxidation products. Consistent with previous studies, no α-pinene dimers were observed by Vocus PTR-TOF at atmospherically relevant α-pinene concentrations (Riva et al., 2019;Li et al., 2020;Li et al., 2021), despite many other types of CIMS routinely detecting abundant dimer formation under similar conditions (Zhao et al., 2018;Riva et al., 2019). To explore potential sensitivity limitations, we increased the α-pinene concentration to as high as 1 ppm (signal around 2.0×10^6 cps). As shown in the mass spectra in Fig. 2a, only four different oxygen-containing ions with carbon number around 20 were observed, although at extremely low concentrations, with the molecular formulae of $C_{18}H_{30}O_2$, $C_{20}H_{30}O_1$, $C_{20}H_{30}O_2$, and $C_{20}H_{32}O_3$. It is hard to speculate how such compositions would arise from the ozonolysis or OH oxidation of the precursor molecule without additional in-source reactions. The production of $C_{20}H_{32}H^+$, which was also observed, was most probably caused by the secondary association reactions between protonated α-pinene with α-pinene in the FIMR. A previous study by Bernhammer et al. (2018) has observed unexpected ion signals of $C_{10}H_{16}H^+$ and $C_{20}H_{32}H^+$ during pure isoprene oxidation. Similar to the results of Bernhammer et al. (2018), the signals of $C_{20}H_{32}H^+$ show a quadratic dependency on the signals of $C_{10}H_{16}H^+$ in our study (Fig. S1).

During the experiment, α-pinene signals varied from 0.5×10^6 cps to 2.0×10^6 cps and then to 0.2×10^6 cps due to changing the injection (Fig.2b). Correspondingly, significant variations were observed for the C_{10} monomers from α-pinene oxidation (i.e., $C_{10}H_{16}O_2$, $C_{10}H_{16}O_3$, $C_{10}H_{14}O_5$, and $C_{10}H_{14}O_6$). However, for the observed oxygenated compounds with carbon number around 20 (i.e., $C_{18}H_{30}O_2$ and $C_{20}H_{30}O_2$), only noisy signals were detected even when α-pinene concentrations reached 1 ppm (i.e., signal ~2.0×10^6 cps). It is possible that all the signals observed in the dimer range are simply clusters formed in the FIMR, similar to $C_{20}H_{32}H^+$. We also emphasize that the poor detection of signals in the region of potential α-pinene dimers in the Vocus PTR-TOF is not merely caused by a low transmission of ions with larger masses. This is for example seen from data from a subsequent study using the same chamber and Vocus PTR-TOF, where the diterpene kaurene ($C_{20}H_{32}$) was oxidized, and we saw significant signals of C_{19} and C_{20} oxidation products (i.e., $C_{19}H_{30}O$ and $C_{20}H_{32}O_3$) from Vocus PTR-TOF measurements (Fig. S2). If the lack of dimers is due to fragmentation, these fragments will most likely overlap with larger signals from monomers, and therefore the very minor contribution of potential dimers to the mass spectrum remains the main experimental result. Similarly, since only the elemental composition of the ions is known, we cannot draw any conclusions on the fates of ROOH species, except to say that we did not detect any signals from typical HOMs as commonly observed by the nitrate CI-APi-TOF.

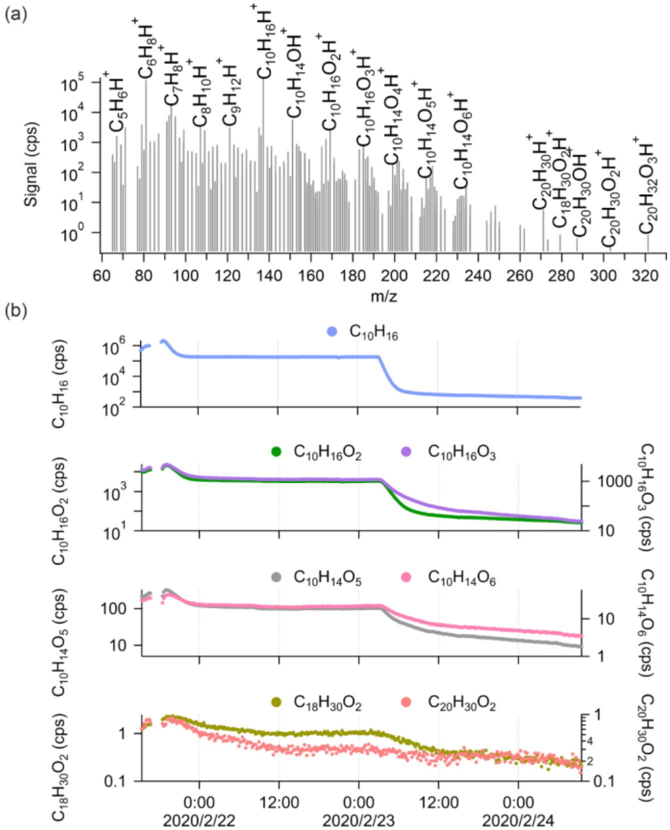

Figure 2. (a) The average mass spectrum of Vocus PTR-TOF measurements during α-pinene (average concentration of 82.4 ± 148.8 ppb) ozonolysis in log scale. The peaks of α-pinene, its major fragments inside the Vocus PTR-TOF, and some α-pinene oxidation products are labelled in the spectrum. (b) Time series of α-pinene ($C_{10}H_{16}$) and its oxidation products during the experiment, including α-pinene monomers ($C_{10}H_{16}O_2$, $C_{10}H_{16}O_3$, $C_{10}H_{14}O_5$, and $C_{10}H_{14}O_6$) and potential α-pinene dimers ($C_{18}H_{30}O_2$ and $C_{20}H_{30}O_2$). α-pinene signals were varied by changing the injection.

3.2 Oxidation products from cyclohexene ozonolysis

We further performed cyclohexene (C_6H_{10}) ozonolysis experiments ([cyclohexene] = 18.7 ± 13.1 ppb; [O_3]= 26.4 ± 9.3 ppb) in the chamber to explore the detection of dimers by Vocus PTR-TOF with a simpler system. From the average mass spectrum in Fig. 3a, $C_5H_6H^+$ and $C_6H_8H^+$ are the most abundant fragments of cyclohexene inside the Vocus PTR-TOF. The variations of $C_5H_6H^+$ and $C_6H_8H^+$ correlated closely with those of cyclohexene during the experiment. Cyclohexene oxidation products with varying oxidation degrees were observed, with the number of oxygen atoms ranging from one to six (Fig. 3a). More oxygenated compounds with nO>6 have previously been seen from cyclohexene ozonolysis using iodide, nitrate, and NH_4^+ CIMS (Iyer et al., 2017;Hansel et al., 2018;Rissanen et al., 2014).

Only two potential cyclohexene dimers were clearly detected by Vocus PTR-TOF, $C_{12}H_{20}O_4$ and $C_{12}H_{22}O_4$. The signal intensities were clearly lower than those of the most abundant monomeric species, but the difference was not as large as in the case of α-pinene. As displayed in Fig. 3b, the $C_{12}H_{22}O_4$ signal was around seven times higher than that of $C_{12}H_{20}O_4$, and considering the standard dimer-forming reaction, $RO_2 + RO_2 \rightarrow ROOR + O_2$, $C_{12}H_{22}O_4$ can be formed by the reaction of two $C_6H_{11}O_3$ peroxy radicals. The $C_6H_{11}O_3$ radical has been previously detected as a major RO_2 radical from cyclohexene ozonolysis in the absence of an OH scavenger (Iyer et al., 2017;Hansel et al., 2018). It is the main expected OH-derived RO_2, following OH addition to the double bond and subsequent addition of O_2. Ozone-derived RO_2 would contain fewer H-atoms, and should be more abundant in this system, but no such dimeric compounds were observed. The time series of $C_{12}H_{20}O_4$ and $C_{12}H_{22}O_4$ showed high similarities to those of monomeric oxidation products, with correlation coefficients (r^2) of mostly larger than 0.9, which is higher than their correlation coefficient with cyclohexene itself. As in the case of α-pinene, we cannot separate any potential dimer fragments from the mass spectra, since all the oxidation products have very high correlations with each other. We can also note that the lack of dimers cannot be attributed to low transmission in the dimer range, as the cyclohexene dimers (C_{12}) are similar in mass as α-pinene monomers (C_{10}).

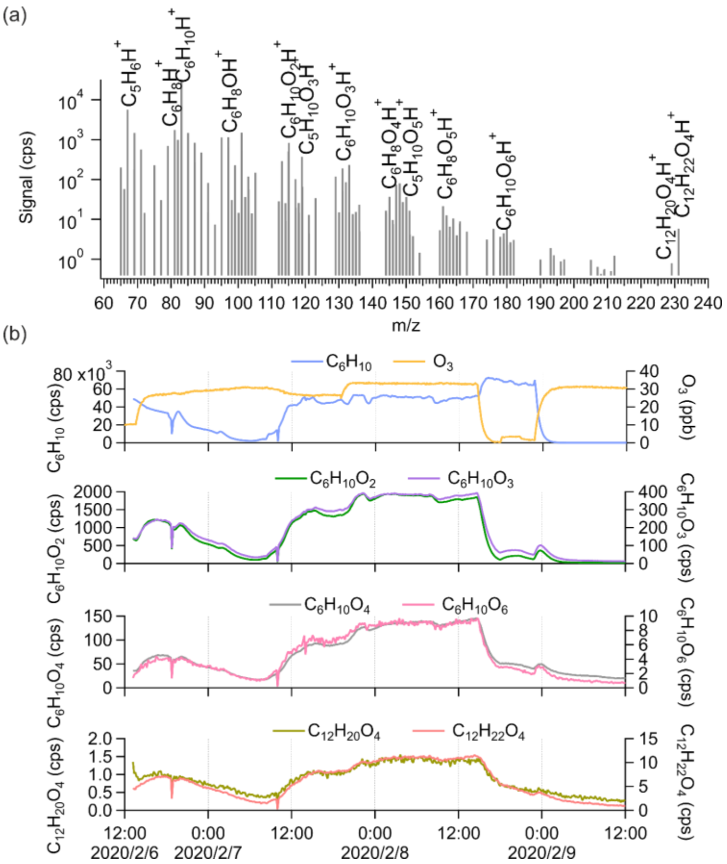

Figure 3. (a) The average mass spectrum of Vocus PTR-TOF measurements from cyclohexene ozonolysis. The peaks of cyclohexene, its major fragments inside the Vocus PTR-TOF, and some cyclohexene oxidation products are labelled. (b) Time series of cyclohexene (C_6H_{10}), O_3, cyclohexene monomers ($C_6H_{10}O_2$, $C_6H_{10}O_3$, $C_6H_{10}O_4$, and $C_6H_{10}O_6$), and potential cyclohexene dimers ($C_{12}H_{20}O_4$ and $C_{12}H_{22}O_4$) during the experiment. Cyclohexene signals were varied by changing the injection.

3.3 Influence of ionization settings on dimer detection

To further get insights into the potential fragmentation of dimers inside the Vocus PTR-TOF, we varied the FIMR pressure and DC voltage during the cyclohexene ozonolysis experiments to see their effects on the detection of different compounds. Both of these parameters would impact the frequency and/or energy of collisions between ions and gas molecules inside the FIMR, and thus also affect the fragmentation probability. During steady-state cyclohexene ozonolysis conditions in the chamber, the FIMR pressure was gradually increased from 1.0 mbar to 3.0 mbar with all other instrumental parameters kept constant. The pressure change decreased the overall sensitivity of the instrument, and in Figure 4a we therefore plot the signal intensity of selected compounds normalized to that of $C_6H_{10}H^+$. With the increase of FIMR pressure from 1.0 mbar to 3.0 mbar, we observed relatively higher signals of cyclohexene oxidation products, both monomers and dimers, but lower signals of $C_5H_6H^+$. As discussed in Sect. 3.2, we know that $C_5H_6H^+$ is one of the most abundant fragments of cyclohexene inside the Vocus PTR, and the lower signal at higher FIMR pressure indicates less fragmentation. Therefore, the higher relative signals of oxidation products can be caused by their decreased fragmentation in the instrument. The increase of different species varied significantly as the pressure was increased, with some changing up to three orders of magnitude relative to cyclohexene. This may indicate differences in their vulnerability to fragment under these FIMR conditions.

Comparatively, FIMR DC voltage had a negligible effect on the ion fragmentation pattern. The DC voltage is placed across the ends of the glass tube of the FIMR to establish the axial electric field in the reactor (Krechmer et al., 2018). In this test, we kept the FIMR pressure constant at 1.4 mbar and gradually decreased the DC voltage from 500 V to 450 V. Since the varied voltages showed no obvious influence on the observations, values lower than 450 V were not probed. As illustrated in Fig. 4b, the relative signal intensity of different compounds changed very little with varying DC voltage. For cyclohexene dimers, we observed only a slight increase in their relative signal intensity at lower DV voltage, but this may also be caused by a small change in the overall mass-dependent transmission of the system.

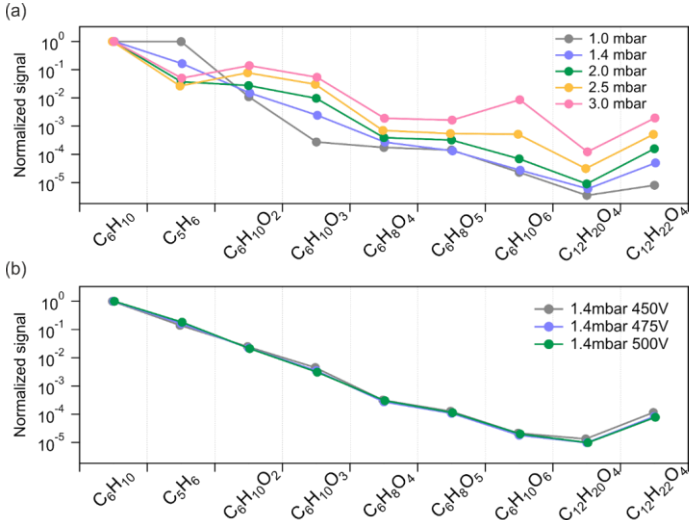

Figure 4. Influence of instrumental settings on the detection of cyclohexene oxidation products by (a) varying FIMR pressures and (b) varying FIMR DC voltages. The y-axis is the signal intensity of different compounds normalized to that of cyclohexene at each condition.

3.4 Computational results

The experiments showed only very minor signals of potential dimers in the Vocus PTR, and this may be indicative of fragmentation inside the instrument during protonation and ion transport. To assess the role of fragmentation in explaining the lack of dimer signals, we calculated the survival probabilities of selected ROOR and ROOH species under conditions in the Vocus FIMR. Computations were first performed on the simplest compounds in order to understand the potential fragmentation reactions. The general reaction mechanism found for gas-phase decomposition of protonated peroxides (ROOR' and ROOH) is shown in Figures 5 and 8. Not all of the reaction steps presented are available to each of the studied systems. Except for **R1b**, **R1c**, **R2b** and their subsequent steps, all reaction steps shown in Figures 5 and 8 had already been reported for the MeOOMe and MeOOH systems by ~~Schalley et al.~~ Schalley et al. (1997).

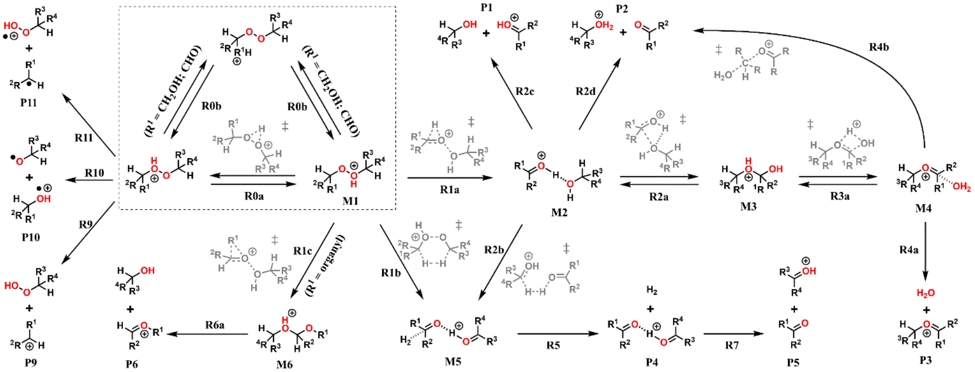

Figure 5. General mechanism for the decomposition of ROOR following protonation. Species within the dashed box are the initial protonation isomers. Transition states are shown in gray. Some pathways are not available for every ROOR investigated. Compound-specific pathways with yields less than 0.1% for any conditions are omitted for clarity.

No transition state was found for reaction with H_3O^+, so each unique oxygen atom was considered to be a possible protonation site, as long as the reaction is exothermic. This leads to the formation of multiple protonation isomers (dashed box in Figures 5 and 8) if the peroxide is asymmetrical (R≠R') and/or carries oxygenated substituents. Proton transfer between the adjacent peroxyl-oxygen atoms (step **R0a**) in general has very high barriers (~30 and ~25 kcal mol^{-1} for ROOR and ROOH respectively), meaning rates of interconversion between protonation isomers are slow compared to other reaction steps. This may change if an oxygenated substituent is present, since very low or no reaction barriers were observed from calculations involving proton transfer to and from these groups (steps **R0b**). In these cases, interconversion between different protonation isomers occurs at very short time scales (tautomerism), and they may be considered to be in a Boltzmann distribution. Nevertheless, the possible reaction pathways that were found to be available for each unique protonation isomer were explored.

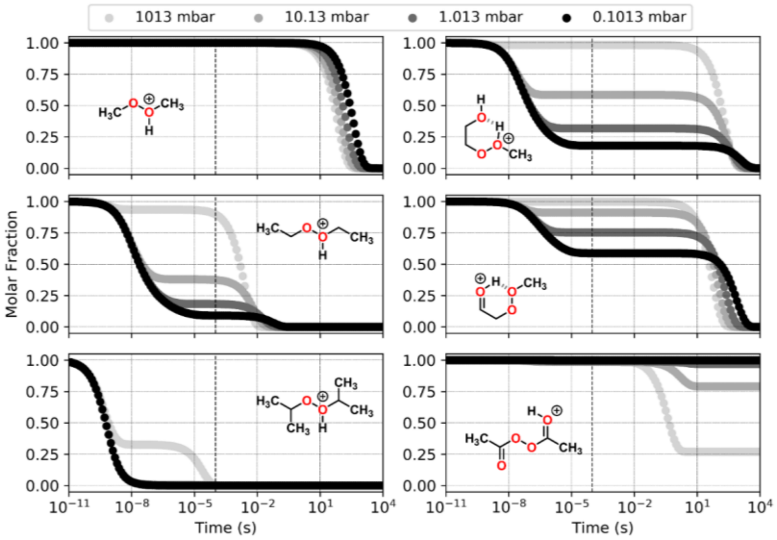

Figure 6. Reaction dynamics simulation results for model ROOR systems. Graphs represent the time evolution profile of initial protonated reactants due to fragmentation, at 298.15 K. Left-hand side, from top to bottom: MeOOHMe$^+$, EtOOHEt$^+$ and iPrOOHiPr$^+$; Right-hand side, from top to bottom: HOEtOOHMe$^+$, HO=EtOOMe$^+$ and AcOOAcH$^+$(Z). Dashed line indicates 100 µs from the start of the simulation.

Results from reaction dynamics simulations are shown in Figure 6 and 7 as time-dependent molar fraction profiles of the initial protonated reactant and its (non-fragmentation) isomerization products at different pressures. Most of the shown time profiles present two different stages of reactant molar fraction decay. The earliest stage corresponds to reactions occurring with species carrying excess energy from the preceding (protonation) reaction step, before significant collisional redistribution of energy. With increasing pressure, collisions with bath gas molecules become more frequent, and a smaller proportion of the reactant goes on to form products during this stage. The latter stage corresponds to reactions occurring at thermal rates, when activating collisions with bath gas molecules may be rate limiting, resulting in a positive pressure dependence. These results likely represent a lower limit for (ROOR)H$^+$ and (ROOH)H$^+$ fragmentation, since the only excess internal energy that was assigned to the initial reactant in these calculations is released during its protonation. In reality, the charged species are generated within a strong electric field, which propels them to supra-thermal speeds. Under this condition, collisions with bath gas molecules have the potential to introduce even more excess internal energy into the reacting system. The following sections will explore the results obtained under this lower limit scenario, while the influence of additional energetic collisions is discussed in the last section.

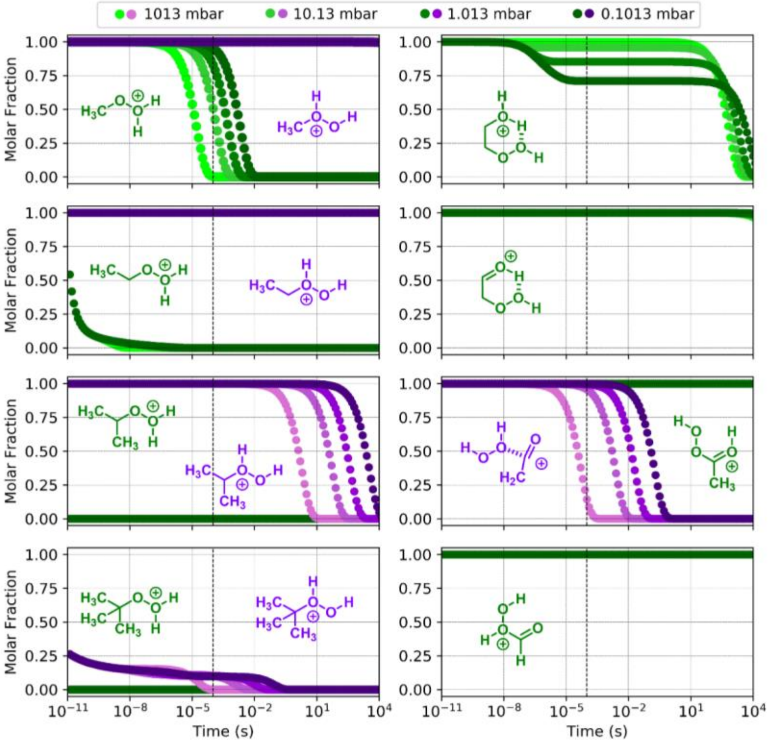

Figure 7. Reaction dynamics simulation results for model ROOH systems. Graphs represent the time evolution profile of fragmentation of initial protonated reactants, at 298.15 K. Left-hand side, from top to bottom: (MeOOH)H$^+$, (EtOOH)H$^+$, (iPrOOH)H$^+$ and (tButOOH)H$^+$; Right-hand side, from top to bottom: (HOEtOOH)H$^+$, (O=EtOOH)H$^+$, (AcOOH)H$^+$ and (OCHOOH)H+. When two protonation isomers that do not readily interconvert are possible, they are plotted in the same graph with different colors (green and purple). Dashed line indicates 100 µs from the start of the simulation.

3.4.1 Model ROOR' systems

Comparing the results for the alkyl substituted ROOR (Figure 6 and Table 1), faster rates of decomposition (thermal and non-thermal) are observed with increasing degree of substitution (R = Me < R = Et < R = iPr). While >99% of the MeOOMe may survive long enough after protonation to be detected by the mass spectrometer, only ~18% of EtOOEt and virtually none of iPrOOiPr is left after 100 µs, at 1.013 mbar. This is due to a combination of larger exothermicity of protonation by H_3O^+ and lower barrier heights for the initial decomposition steps **R1a** and **R1c**, as seen in Figure S6 and Table S1. The first of these factors may be explained by the greater electronic density introduced into the peroxy oxygens by methyl groups via inductive effects, increasing the proton affinity of the peroxide. The second factor can be understood by invoking hyperconjugative stabilization of the transition states of steps **R1a** and **R1c**. Detailed description of the fragmentation mechanisms and analysis of their energetics is found in the Supplementary Information.

As for the systems containing oxygenated substituents, HOEtOOMe and O=EtOOMe, relatively less fragmentation was observed within relevant time scales. At 1.013 mbar, ~68.2% of HOEtOOMe and ~24.6% of O=EtOOMe are left intact after 100 μs, the major fragmentation product being **P6** in both cases. As described in the beginning of this section, interconversion between the initial protonation isomers was found to be fast. Very low-lying transition states were found for steps **R0b** in the PES of HOEtOOMe, whereas no transition states were found for the O=EtOOMe counterparts. Thus, for the sake of analysis of the rate of decomposition of these two peroxides, all of their initial reaction step transition states can be assumed to be connected to their most stable protonation isomer, HOEtOO**H**Me$^+$ and **H**O=EtOOMe$^+$, shown in Figure S7. The reaction of protonated AcOOAc, which follows a different mechanism, is shown through its PES in Figure S8. The calculations show that after 100 μs, at 1.013 mbar and 298.15 K, about 18% of protonated AcOOAc is converted to protonated acetic methylcarbonic anhydride (AMCAH$^+$) and ~1% yields fragmentation products AcOOH + Ac$^+$. However, in this case the major product AMCAH$^+$ has the same elemental composition as the reactant, and therefore the mass spectrum would not be considerably impacted. Fragmentation in this system seems to be favored by increasing pressures, as seen from Figure 6, but we emphasize again that we are now only considering conditions without electric fields causing additional energy to be absorbed through energetic collisions.

With the exception of AcOOAc, the final charged products formed in the decomposition of the model ROOR systems are fragments of the parent molecule, and therefore the signal produced in the mass spectrometer detector would correspond to a different elemental composition. Fragmentation percentage and product distribution for each of these systems are shown in Table 1.

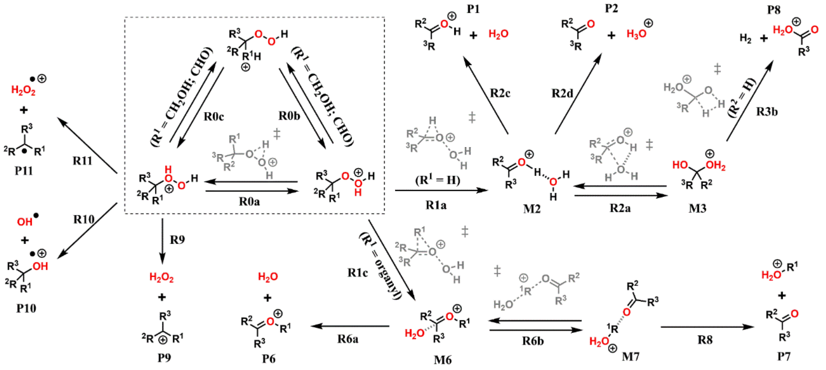

Figure 8. General mechanism for the decomposition of ROOH following protonation. Species within the dashed box are the initial protonation isomers. Transition states are shown in gray. Some pathways are not available for every ROOH investigated. Compound-specific pathways with yields less than 0.1% are omitted for clarity.

3.4.2 Model ROOH systems

As seen from Figure S9, interconversion between the protonation isomers of alkyl-substituted hydroperoxides (RO**H**OH$^+$ and ROO**H**$_2^+$) shows very high reaction barriers (23~26 kcal·mol^{-1}) and therefore the two initial reactant species must be considered separately. The ROO**H**$_2^+$ protonation isomers showed faster fragmentation rates than their peroxide 'dimer' (ROOR)**H**$^+$ analogues, but both were observed to follow a very similar trend in reactivity. The energy released during protonation by H_3O^+ is considerably smaller for ROOH systems, which could reduce the proportion of molecules that react at non-thermal rates. On the other hand, the barrier heights for the steps **R1a** and **R1c** are also lower, meaning thermal reaction rates are faster. Given that any of the considered R groups have a greater electron-donating effect than a hydrogen, a ROOH system has a smaller proton affinity but its O-O bond is more polarized compared to a ROOR. Fragmentation percentages and product distributions are shown in Table 1. In contrast, protonation isomer RO**H**OH$^+$ is rather inert. Apart from isomerization into ROO**H**$_2^+$, only the three direct dissociation channels (**R9**, **R10** and **R11**) are available to these species. Each of these channels was investigated but, except for **R8** with tButO**H**OH$^+$, none were observed to contribute to fragmentation within significant timescales, under the lower limit of excess energy scenario. At 1.013 mbar, about 89.8% of tButO**H**OH$^+$ fragments into tert-butyl cation + H_2O_2 within 100 μs, while other RO**H**OH$^+$ remain unreacted in the absence of energetic collisions. Decomposition of the protonated peroxy acids follows a different mechanism, described in detail in the SI. The calculations predict the fragmentation of only ~0.6% of protonated peracetic acid after 100 μs, at 1.013 mbar. No reaction was predicted to occur for protonated performic acid.

Table 1. Species distribution of each studied ROOR and ROOH obtained from reaction dynamics simulation after 100 μs, at 298.15 K and 1.013 mbar. Results are shown for two scenarios differing in the amount of excess internal energy (E_{ex}) assigned to the initial reactant: 1) Only protonation energy ($E_{ex} = \Delta E_{zp,prot}$); 2) Protonation energy plus reference energy value from high-speed collisions ($E_{ex} = \Delta E_{zp,prot}$ + 0.5 eV). Percentage of unreacted ROOR and ROOH highlighted in bold. [a]: AMCAH$^+$ is an isomer of the original protonated peroxide. [b]: End product of channel R1d, shown in the SI.

(ROOR)H$^+$	**Species distribution after 100 μs (T = 298.15 K; p = 1.013 mbar)**	
	Low-limit scenario ($E_{ex} = \Delta E_{zp,prot}$)	**Energetic collision scenario ($E_{ex} = \Delta E_{zp,prot}$ + 0.5 eV)**
Me-OO**H**-Me$^+$	ROOR **(>99.9%)**	ROOR **(61.2%)**, P1 (35.3%), P2 (3.4%)
Et-OO**H**-Et$^+$	ROOR **(18.3%)**, P6 (55.5%), P2 (21.2%), P1 (4.4%), P3 (0.5%)	ROOR **(0.2%)**, P6 (80.4%), P2 (15.6%), P1 (3.3%), P3 (0.5%)
iPr-OO**H**-iPr$^+$	ROOR **(~0%)**, P6 (55.1%), P2 (32.1%), P1 (12.7%)	ROOR **(~0%)**, P6 (58.1%), P2 (30.8%), P1 (11.1%)
HOEt-OO**H**-Me$^+$	ROOR **(31.8%)**, P6 (68.2%)	ROOR **(1.4%)**, P6 (98.4%), P1 (0.1%), P2 (0.1%)
HO=Et-OO-Me$^+$	ROOR **(75.4%)**, P6 (24.6%)	ROOR **(4.4%)**, P6 (95.6%)
Ac-OO-Ac**H**(Z)$^+$	ROOR **(80.7%)**, AMCAH$^+$ (18.4%)[a], AcOOH + Ac$^+$ (0.9%)	ROOR **(1.8%)**, AMCAH$^+$ (3.8%)[a], AcOOH + Ac$^+$ (94.4%)
(Cyclohexene + OH)	ROOR **(6.2%)**, P10 (92.4%), P9 (1.3%)	ROOR **(~0%)**, P10 (95.4%), P9 (4.5%)
(Cyclohexene + O_3)	ROOR **(0.1%)**, P10 (15.4%), P9 (84.3%), P2[b] (0.2%)	ROOR **(~0%)**, P10 (43.9%), P9 (56.1%)

(ROOH)H$^+$		
Me-OO**H**-H$^+$	ROOH **(83.0%)**, P2 (9.3%), P1 (7.7%)	ROOH **(83.0%)**, P2 (9.3%), P1 (7.7%)
Me-**H**OO-H$^+$	ROOH **(>99.9%)**	ROOH **(>99.9%)**
Et-OO**H**-H$^+$	ROOH **(~0%)**, P3 (>99.9%)	ROOH **(~0%)**, P6 (>99.9%)
Et-**H**OO-H$^+$	ROOH **(>99.9%)**	ROOH **(>99.9%)**
iPr-OO**H**-H$^+$	ROOH **(~0%)**, P3 (96.8%), P2 (3.2%)	ROOH **(~0%)**, P6 (96.6%), P2 (3.4%)
iPr-**H**OO-H$^+$	ROOH **(>99.9%)**	ROOH **(38.7%)**, P9 (61.3%)
tBut-OO**H**-H$^+$	ROOH **(~0%)**, P3 (>99.9%)	ROOH **(~0%)**, P6 (>99.9%)
tBut-**H**OO-H$^+$	ROOH **(10.2%)**, P9 (89.8%)	ROOH **(0.1%)**, P9 (99.9%)
H_2OEt-OO-H$^+$	ROOH **(85.3%)**, P6 (14.6%)	ROOH **(7.9%)**, P6 (84.6%), P1 (6.9%), P2 (0.6%)
HO=Et-OO-H$^+$	ROOH **(>99.9%)**	ROOH **(74.5%)**, P6 (25.5%)
HAc-OO-H$^+$	ROOH **(>99.9%)**	ROOH **(>99.9%)**
Ac$^+$:**H_2**O_2	ROOH **(99.4%)**, Ac$^+$ + H_2O_2 (0.6%)	ROOH **(24.8%)**, Ac$^+$ + H_2O_2 (75.2%)
HOCH-OOH$^+$	ROOH **(>99.9%)**	ROOH **(>99.9%)**
(Cyclohexene + OH)	ROOH **(0.1%)**, P9 (99.5%), P6 (0.4%)	ROOH **(~0%)**, P9 (99.6%), P6 (0.4%)
(Cyclohexene + O_3)	ROOH **(0.1%)**, P9 (99.9%)	ROOH **(~0%)**, P9 (>99.9%)

3.4.3 Cyclohexene oxidation products

Following the model peroxide molecules, calculations were done to assess whether ROOR and ROOH species produced during oxidation of cyclohexene are expected to suffer rapid fragmentation following protonation. The investigated peroxides, shown in Figure 1, are produced from first-generation peroxy radical intermediates of oxidation by OH and O_3. Oxidation by OH radical would be initiated by electrophilic attack on the C-C π bond, with subsequent O_2 addition to the radical center carbon, producing a cyclic β-hydroxy alkylperoxy radical (Aschmann et al., 2012). The formation of the ozonolysis-derived peroxy radical precursor considered here follows a more complicated mechanism, which is described in detail by e.g. Rissanen et al. (2014). The hydrocarbon ring is opened during oxidation by O_3, resulting in a linear β-oxo alkylperoxy radical.

In all peroxides considered here, the peroxyl group's adjacent C is secondary, and thus the barrier for reaction steps **R1a** and **R1c** would be expected to be low as observed in iPrOOiPr and iPrOOH systems. On the other hand, these peroxides are also (at least) β-substituted with O-bearing functionalities, which can be more energetically favorable protonation sites and/or enable the formation of stabilizing intramolecular H-bonds. As a result, barriers to reaction step **R1a** encountered by these cyclohexene oxidation products are high, but in general 1~3 kcal ~~-~~·mol^{-1} lower in comparison to HOEt- and O=Et- substituted model systems. This value is very similar to the difference in **R1a** barrier height between iPr- and Et- substituted systems. Concerning **R1c**, the ROOR systems encounter barriers which are 4~5 kcal ~~-~~·mol^{-1} higher in comparison with model systems, while the opposite trend is observed for ROOH species. This may be due to the added stability brought to the reactant by the larger R- groups, which would be stronger in the ROOR systems compared to the ROOH systems. A new channel (**R1d**) was found for the cyclohexene + O_3 products, where the O-O bond scission occurs with concerted 1,6 ~~H~~H^+ ~~-~~transfer to the far carbonyl-oxygen, shown in Figure S12. The produced fragments are the same as those resulting from **R1a**, but this step involves a more favorable rearrangement, thus showing a ~6 kcal·mol^{-1} lower barrier. The PES calculated for the decomposition of these systems is shown in Figures S13-S14.

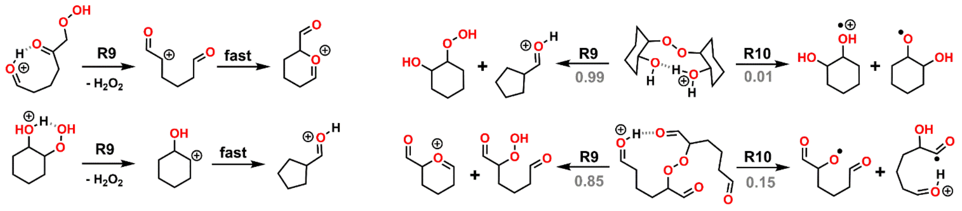

Figure 9. Major reaction channels for decomposition of ROOH (left) and ROOR (right) obtained from OH oxidation and ozonolysis of cyclohexene. Branching ratios are shown in gray when relevant.

Nevertheless, the calculations revealed that the most favorable fragmentation pathways for these systems are **R9** and **R10**, involving direct dissociation of the initial reactant, without any concomitant rearrangement. The energy required for these channels is still high, like the ones observed for the model systems, but it is offset by the much larger energy released during protonation. Results from reaction dynamics simulations (Figure 10) showed that at 1.013 mbar, almost all (99.6%) of the ROOR derived from ozonolysis fragments within ~1 µs following protonation, the major products being **P9** (84.0%) and **P10** (15.4%). About 6.2% of the ROOR derived from OH oxidation survives unreacted after 100 µs, the major products being **P10** (92.4%) and **P9** (1,3%). Virtually all (99.9%) of the ROOH, derived from either ozonolysis or OH oxidation, is predicted to fragment within ~1 µs, leading to the heterolysis products (**P9**). The cationic fragment produced by **R9** suffers rearrangement after dissociation. During geometry optimization, those species spontaneously undergo isomerization into the systems shown in the right-hand side of the ROOH decomposition mechanisms in Figure 9.

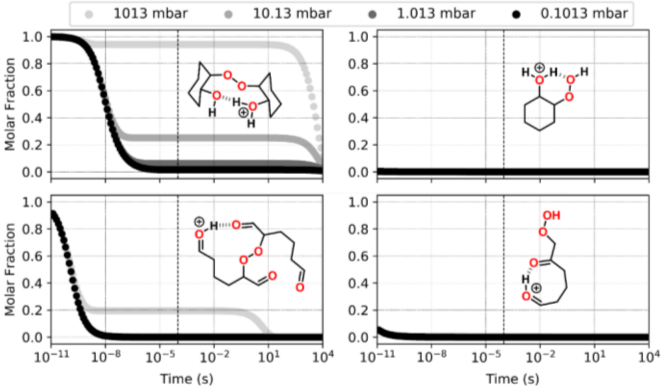

Figure 10. Reaction dynamics simulation results for the investigated ROOR (left) and ROOH (right) species derived from cyclohexene oxidation by OH radical (top) and O_3 (bottom). Graphs represent the time evolution profile for reaction of initial protonated reactants, at 298.15 K. Dashed line indicates 100 µs from the start of the simulation.

3.4.4 High energy collisions

In order to validate the computational methods, the same set of calculations was done with the decomposition of n-butanol following protonation in the gas phase. In an experiment conducted with this compound in the Vocus PTR, the signal corresponding to $C_4H_9^+$ was observed to be 100 times higher than the signal from the initial charged species $C_4H_{10}OH^+$. The investigated decomposition mechanism is analogous to the one reported for protonated ethanol (Swanton et al., 1991), where the major reaction pathways lead to H_2O or H_3O^+ elimination. The calculated PES and reaction dynamics simulation results are shown in Figures S15-S16. The calculations predicted that at 1.013 mbar, only about 48% of n-butanol fragments into 2-butyl cation ($C_4H_9^+$) + H_2O after 100 µs, suggesting that excess energy from protonation alone is not enough to account for fragmentation in the Vocus PTR. High energy collisions provoked by the strong electric field present within the instrument may explain this difference. When assigning an additional 0.5 eV of excess energy to the initial charged reactant on top of the protonation energy, the simulation predicts fragmentation of 98% of protonated n-butanol molecules. This result is much closer to what is observed experimentally, and an energy value of 0.5 eV may serve as a qualitative reference of excess energy derived from supra-thermal speed collisions. With an additional 0.5 eV excess energy, the simulations predict that most of the studied ROOR and ROOH systems fragment significantly within 100 µs, as shown in Table 1. Time evolution profiles of fragmentation under these conditions are shown in Figures S17-18.

4 Conclusions

Both computational (Hyttinen et al., 2018) and experimental (Riva et al., 2019) studies have shown that the selectivity of different types of chemical ionization mass spectrometers used in atmospheric chemistry varies considerably. Many of the differences have been attributed to how strongly molecules with different functionalities will bind to the reagent ions, or how favorable a charge transfer from reagent ions to sample molecules are. However, in certain cases this has not been enough to explain observations, and one such example has been the lack of gas-phase dimeric species observable with many PTR instruments, such as the Vocus PTR. In this work, we evaluated the dimer detection both experimentally and through computations.

In the case of α-pinene ozonolysis, a system where e.g. nitrate- and iodide-based CIMS have detected large concentrations of dimers, no verifiable dimer oxidation products were detected with the Vocus PTR-TOF, in agreement with earlier work. A slightly larger, though still marginal, fraction of dimers was observed from the ozonolysis of cyclohexene. The lack of dimers could not be explained by low mass-transmission at the dimer masses, since signals were observed in this range from monomeric oxidation products. The low volatility of any oxygenated dimer species may have further decreased the likelihood of detection, but given that fragmentation is a common observation in PTR systems, the importance of decomposition reactions remained a viable hypothesis.

With this starting point, we computed the fragmentation pathways and corresponding rates of different peroxide dimers, ROOR. The general trend showed that the smallest ROOR like methyl peroxide showed very little fragmentation following the additional excess energy received upon protonation and the following thermalized collisions, but with increased substitutions and functionalization, more fragmentation was observed. When adding an additional 0.5 eV excess energy to the molecules, as an estimate of the energy absorbed due to energetic ion-molecule collisions driven by the electric fields in the Vocus ionization region, the vast majority of ROOR dimers were expected to fragment within the 100 µs residence time in this region. The electric fields in the PTR-MS instruments, including the Vocus PTR, are used for guiding and declustering ions, but come with the drawback of enhancing fragmentation reactions for certain species. These results are in good agreement with the observed lack of dimers in the Vocus PTR.

We also performed similar calculations on ROOH hydroperoxides, finding that most of these molecules were also expected to fragment nearly to 100 % under the conditions of the Vocus PTR. The result is harder to verify experimentally, as the mass spectrometric techniques cannot separate between functional groups within molecules. However, earlier studies have shown that other adduct-forming CIMS types tend to detect more oxygenated species than the Vocus PTR (Riva et al., 2019), lending support to the computational findings of this work. Importantly, our results suggest that the protonation of ROOR and ROOH species does not automatically lead to total fragmentation. However, the added energy from the ion-molecule collisions caused by electric fields, used for ion guiding or declustering, can add considerably to the fraction of ions undergoing fragmentation. For the Vocus PTR-TOF used in this study, we predict nearly complete fragmentation for almost all studied chemically-labile peroxide species. Attempts to model this theoretically and/or computationally using molecular dynamics or other models are a major challenge, since bond breaking processes must be treated explicitly. Very recently some new methods have been introduced which use *ab initio* molecular dynamics (AIMD) to model collision induced dissociation (CID) in mass spectrometry (Koopman and Grimme, 2021;Schreckenbach et al., 2021). Adapting these methods to model ion fragmentation in PTR based mass spectrometry would be a fruitful avenue for further research.

PTR-based mass spectrometers are powerful tools for measuring volatile emissions, and newer generation instrument like the Vocus PTR are able to measure also many oxidation products of these emissions. However, the most oxygenated species and the dimeric species evade detection in most PTR instruments, due to losses caused both by condensation and fragmentation. As such, other CIMS types are likely better suited for the detection of these types of species, though the stability of ions with different functionalities may be worth further study also in these instruments.

Data availability. Data are available for scientific purposes upon request to the corresponding authors.

Author Contributions. ME and HL conceived the study. HL conducted the chamber experiments. TGA and CDD performed the quantum chemical calculations with the assistance of TK. YL, JZ, WH and CM helped with the measurements. HL and TGA carried out the data analysis. HL, TGA, and ME wrote the paper. All authors commented on the paper.

Competing interests. The authors declare that they have no conflict of interest.

Acknowledgments. This research has been supported by the H2020 European Research Council (grant nos. COALA (638703), ATM-GTP (742206), and CHAPAs (850614)) and the Academy of Finland (grant nos. 317380, 320094, and 1315600). Haiyan Li acknowledges financial support from the Jenny and Antti Wihuri Foundation. The authors would also like to thank the Knut and Alice Wallenberg Foundation for financial support (WAF project CLOUDFORM, grant no. 2017.0165).

References

Aprea, E., Biasioli, F., Märk, T. D., and Gasperi, F.: PTR-MS study of esters in water and water/ethanol solutions: Fragmentation patterns and partition coefficients, International Journal of Mass Spectrometry, 262, 114-121, https://doi.org/10.1016/j.ijms.2006.10.016, 2007.

Aschmann, S. M., Arey, J., and Atkinson, R.: Kinetics and Products of the Reactions of OH Radicals with Cyclohexene, 1-Methyl-1-cyclohexene, cis-Cyclooctene, and cis-Cyclodecene, The Journal of Physical Chemistry A, 116, 9507-9515, 10.1021/jp307217m, 2012.

Barker, J. R.: Energy transfer in master equation simulations: A new approach, International Journal of Chemical Kinetics, 41, 748-763, https://doi.org/10.1002/kin.20447, 2009.

Barker, J. R., and Weston, R. E.: Collisional Energy Transfer Probability Densities P(E, J; E′, J′) for Monatomics Colliding with Large Molecules, The Journal of Physical Chemistry A, 114, 10619-10633, 10.1021/jp106443d, 2010.

Becke, A. D.: A new mixing of Hartree-Fock and Local Density-Functional Theories, J. Chem. Phys., 98, 1372-1377, 10.1063/1.464304, 1993.

Berndt, T., Mentler, B., Scholz, W., Fischer, L., Herrmann, H., Kulmala, M., and Hansel, A.: Accretion Product Formation from Ozonolysis and OH Radical Reaction of α-Pinene: Mechanistic Insight and the Influence of Isoprene and Ethylene, Environmental Science & Technology, 52, 11069-11077, 10.1021/acs.est.8b02210, 2018a.

Berndt, T., Scholz, W., Mentler, B., Fischer, L., Herrmann, H., Kulmala, M., and Hansel, A.: Accretion Product Formation from Self- and Cross-Reactions of RO2 Radicals in the Atmosphere, Angewandte Chemie International Edition, 57, 3820-3824, https://doi.org/10.1002/anie.201710989, 2018b.

Bernhammer, A. K., Fischer, L., Mentler, B., Heinritzi, M., Simon, M., and Hansel, A.: Production of highly oxygenated organic molecules (HOMs) from trace contaminants during isoprene oxidation, Atmos. Meas. Tech., 11, 4763-4773, 10.5194/amt-11-4763-2018, 2018.

Bertram, T. H., Kimmel, J. R., Crisp, T. A., Ryder, O. S., Yatavelli, R. L. N., Thornton, J. A., Cubison, M. J., Gonin, M., and Worsnop, D. R.: A field-deployable, chemical ionization time-of-flight mass spectrometer, Atmos. Meas. Tech., 4, 1471-1479, 10.5194/amt-4-1471-2011, 2011.

Bianchi, F., Kurtén, T., Riva, M., Mohr, C., Rissanen, M. P., Roldin, P., Berndt, T., Crounse, J. D., Wennberg, P. O., Mentel, T. F., Wildt, J., Junninen, H., Jokinen, T., Kulmala, M., Worsnop, D. R., Thornton, J. A., Donahue, N., Kjaergaard, H. G., and Ehn, M.: Highly Oxygenated Organic Molecules (HOM) from Gas-Phase Autoxidation Involving Peroxy Radicals: A Key Contributor to Atmospheric Aerosol, Chem Rev, 119, 3472-3509, 10.1021/acs.chemrev.8b00395, 2019.

Breitenlechner, M., Fischer, L., Hainer, M., Heinritzi, M., Curtius, J., and Hansel, A.: PTR3: An Instrument for Studying the Lifecycle of Reactive Organic Carbon in the Atmosphere, Analytical Chemistry, 89, 5824-5831, 10.1021/acs.analchem.6b05110, 2017.

Carter, W. P. L.: Development of Ozone Reactivity Scales for Volatile Organic Compounds, Air & Waste, 44, 881-899, 10.1080/1073161X.1994.10467290, 1994.

Chai, J. D., and Head-Gordon, M.: Long-range corrected hybrid density functionals with damped atom-atom dispersion corrections, Phys. Chem. Chem. Phys., 10, 6615-6620, 10.1039/b810189b, 2008.

Charlson, R. J., Schwartz, S. E., Hales, J. M., Cess, R. D., Coakley, J. A., Hansen, J. E., and Hofmann, D. J.: Climate Forcing by Anthropogenic Aerosols, Science, 255, 423, 10.1126/science.255.5043.423, 1992.

Chen, X., Hopke, P. K., and Carter, W. P. L.: Secondary Organic Aerosol from Ozonolysis of Biogenic Volatile Organic Compounds: Chamber Studies of Particle and Reactive Oxygen Species Formation, Environmental Science & Technology, 45, 276-282, 10.1021/es102166c, 2011.

Crounse, J. D., Nielsen, L. B., Jørgensen, S., Kjaergaard, H. G., and Wennberg, P. O.: Autoxidation of Organic Compounds in the Atmosphere, The Journal of Physical Chemistry Letters, 4, 3513-3520, 10.1021/jz4019207, 2013.

Donahue, N. M., Kroll, J. H., Pandis, S. N., and Robinson, A. L.: A two-dimensional volatility basis set – Part 2: Diagnostics of organic-aerosol evolution, Atmos. Chem. Phys., 12, 615-634, 10.5194/acp-12-615-2012, 2012.

Ehn, M., Thornton, J. A., Kleist, E., Sipilä, M., Junninen, H., Pullinen, I., Springer, M., Rubach, F., Tillmann, R., Lee, B., Lopez-Hilfiker, F., Andres, S., Acir, I.-H., Rissanen, M., Jokinen, T., Schobesberger, S., Kangasluoma, J., Kontkanen, J., Nieminen, T., Kurtén, T., Nielsen, L. B., Jørgensen, S., Kjaergaard, H. G., Canagaratna, M., Maso, M. D., Berndt, T., Petäjä, T., Wahner, A., Kerminen, V.-M., Kulmala, M., Worsnop, D. R., Wildt, J., and Mentel, T. F.: A large source of low-volatility secondary organic aerosol, Nature, 506, 476-479, 10.1038/nature13032, 2014.

Friedrich, R., and Obermeier, A.: Chapter 1 - Anthropogenic Emissions of Volatile Organic Compounds, in: Reactive Hydrocarbons in the Atmosphere, edited by: Hewitt, C. N., Academic Press, San Diego, 1-39, 1999.

Glowacki, D. R., Liang, C. H., Morley, C., Pilling, M. J., and Robertson, S. H.: MESMER: An Open-Source Master Equation Solver for Multi-Energy Well Reactions, J. Phys. Chem. A, 116, 9545-9560, 10.1021/jp3051033, 2012.

Gueneron, M., Erickson, M. H., VanderSchelden, G. S., and Jobson, B. T.: PTR-MS fragmentation patterns of gasoline hydrocarbons, International Journal of Mass Spectrometry, 379, 97-109, https://doi.org/10.1016/j.ijms.2015.01.001, 2015.

Guenther, A. B., Jiang, X., Heald, C. L., Sakulyanontvittaya, T., Duhl, T., Emmons, L. K., and Wang, X.: The Model of Emissions of Gases and Aerosols from Nature version 2.1 (MEGAN2.1): an extended and updated framework for modeling biogenic emissions, Geosci. Model Dev., 5, 1471-1492, 10.5194/gmd-5-1471-2012, 2012.

Halgren, T. A.: MMFF VII. Characterization of MMFF94, MMFF94s, and other widely available force fields for conformational energies and for intermolecular-interaction energies and geometries, J. Comput. Chem., 20, 730-748, 10.1002/(sici)1096-987x(199905)20:7<730::Aid-jcc8>3.3.Co;2-k, 1999.

Hansel, A., Scholz, W., Mentler, B., Fischer, L., and Berndt, T.: Detection of RO2 radicals and other products from cyclohexene ozonolysis with NH4+ and acetate chemical ionization mass spectrometry, Atmos Environ, 186, 248-255, https://doi.org/10.1016/j.atmosenv.2018.04.023, 2018.

Huang, C., Chen, C. H., Li, L., Cheng, Z., Wang, H. L., Huang, H. Y., Streets, D. G., Wang, Y. J., Zhang, G. F., and Chen, Y. R.: Emission inventory of anthropogenic air pollutants and VOC species in the Yangtze River Delta region, China, Atmos. Chem. Phys., 11, 4105-4120, 10.5194/acp-11-4105-2011, 2011.

Hyttinen, N., Kupiainen-Määttä, O., Rissanen, M. P., Muuronen, M., Ehn, M., and Kurtén, T.: Modeling the Charging of Highly Oxidized Cyclohexene Ozonolysis Products Using Nitrate-Based Chemical Ionization, The Journal of Physical Chemistry A, 119, 6339-6345, 10.1021/acs.jpca.5b01818, 2015.

Hyttinen, N., Otkjær, R. V., Iyer, S., Kjaergaard, H. G., Rissanen, M. P., Wennberg, P. O., and Kurtén, T.: Computational Comparison of Different Reagent Ions in the Chemical Ionization of Oxidized Multifunctional Compounds, The Journal of Physical Chemistry A, 122, 269-279, 10.1021/acs.jpca.7b10015, 2018.

Isaacman-VanWertz, G., Massoli, P., O'Brien, R., Lim, C., Franklin, J. P., Moss, J. A., Hunter, J. F., Nowak, J. B., Canagaratna, M. R., Misztal, P. K., Arata, C., Roscioli, J. R., Herndon, S. T., Onasch, T. B., Lambe, A. T., Jayne, J. T., Su, L., Knopf, D. A., Goldstein, A. H., Worsnop, D. R., and Kroll, J. H.: Chemical evolution of atmospheric organic carbon over multiple generations of oxidation, Nat Chem, 10, 462-468, 10.1038/s41557-018-0002-2, 2018.

Iyer, S., He, X., Hyttinen, N., Kurtén, T., and Rissanen, M. P.: Computational and Experimental Investigation of the Detection of HO2 Radical and the Products of Its Reaction with Cyclohexene Ozonolysis Derived RO2 Radicals by an Iodide-Based Chemical Ionization Mass Spectrometer, The Journal of Physical Chemistry A, 121, 6778-6789, 10.1021/acs.jpca.7b01588, 2017.

Jasper, A. W., Pelzer, K. M., Miller, J. A., Kamarchik, E., Harding, L. B., and Klippenstein, S. J.: Predictive a priori pressure-dependent kinetics, Science, 346, 1212-1215, doi:10.1126/science.1260856, 2014.

Jimenez, J. L., Canagaratna, M. R., Donahue, N. M., Prevot, A. S. H., Zhang, Q., Kroll, J. H., DeCarlo, P. F., Allan, J. D., Coe, H., Ng, N. L., Aiken, A. C., Docherty, K. S., Ulbrich, I. M., Grieshop, A. P., Robinson, A. L., Duplissy, J., Smith, J. D., Wilson, K. R., Lanz, V. A., Hueglin, C., Sun, Y. L., Tian, J., Laaksonen, A., Raatikainen, T., Rautiainen, J., Vaattovaara, P., Ehn, M., Kulmala, M., Tomlinson, J. M., Collins, D. R., Cubison, M. J., Dunlea, J., Huffman, J. A., Onasch, T. B., Alfarra, M. R., Williams, P. I., Bower, K., Kondo, Y., Schneider, J., Drewnick, F., Borrmann, S., Weimer, S., Demerjian, K., Salcedo, D., Cottrell, L., Griffin, R., Takami, A., Miyoshi, T., Hatakeyama, S., Shimono, A., Sun, J. Y., Zhang, Y. M., Dzepina, K., Kimmel, J. R., Sueper, D., Jayne, J. T., Herndon, S. C., Trimborn, A. M., Williams, L. R., Wood, E. C., Middlebrook, A. M., Kolb, C. E., Baltensperger, U., and Worsnop, D. R.: Evolution of Organic Aerosols in the Atmosphere, Science, 326, 1525, 10.1126/science.1180353, 2009.

Jokinen, T., Sipilä, M., Junninen, H., Ehn, M., Lönn, G., Hakala, J., Petäjä, T., Mauldin Iii, R. L., Kulmala, M., and Worsnop, D. R.: Atmospheric sulphuric acid and neutral cluster measurements using CI-APi-TOF, Atmos. Chem. Phys., 12, 4117-4125, 10.5194/acp-12-4117-2012, 2012.

Kendall, R. A., Jr., T. H. D., and Harrison, R. J.: Electron affinities of the first-row atoms revisited. Systematic basis sets and wave functions, The Journal of Chemical Physics, 96, 6796-6806, 10.1063/1.462569, 1992.

Kesselmeier, J., and Staudt, M.: Biogenic Volatile Organic Compounds (VOC): An Overview on Emission, Physiology and Ecology, J Atmos Chem, 33, 23-88, 10.1023/A:1006127516791, 1999.

Knizia, G., Adler, T. B., and Werner, H. J.: Simplified CCSD(T)-F12 methods: Theory and benchmarks, J. Chem. Phys., 130, 20, 10.1063/1.3054300, 2009.

Koopman, J., and Grimme, S.: From QCEIMS to QCxMS: A Tool to Routinely Calculate CID Mass Spectra Using Molecular Dynamics, J Am Soc Mass Spectrom, 32, 1735-1751, 10.1021/jasms.1c00098, 2021.

Krechmer, J., Lopez-Hilfiker, F., Koss, A., Hutterli, M., Stoermer, C., Deming, B., Kimmel, J., Warneke, C., Holzinger, R., Jayne, J., Worsnop, D., Fuhrer, K., Gonin, M., and de Gouw, J.: Evaluation of a New Reagent-Ion Source and Focusing Ion–Molecule Reactor for Use in Proton-Transfer-Reaction Mass Spectrometry, Analytical Chemistry, 90, 12011-12018, 10.1021/acs.analchem.8b02641, 2018.

Kupiainen-Määttä, O., Olenius, T., Kurtén, T., and Vehkamäki, H.: CIMS Sulfuric Acid Detection Efficiency Enhanced by Amines Due to Higher Dipole Moments: A Computational Study, The Journal of Physical Chemistry A, 117, 14109-14119, 10.1021/jp4049764, 2013.

Lee, B. H., Lopez-Hilfiker, F. D., Mohr, C., Kurten, T., Worsnop, D. R., and Thornton, J. A.: An Iodide-Adduct High-Resolution Time-of-Flight Chemical-Ionization Mass Spectrometer: Application to Atmospheric Inorganic and Organic Compounds, Environmental Science & Technology, 48, 6309-6317, 2014a.

Lee, B. H., Lopez-Hilfiker, F. D., Mohr, C., Kurtén, T., Worsnop, D. R., and Thornton, J. A.: An Iodide-Adduct High-Resolution Time-of-Flight Chemical-Ionization Mass Spectrometer: Application to Atmospheric Inorganic and Organic Compounds, Environmental Science & Technology, 48, 6309-6317, 10.1021/es500362a, 2014b.

Lee, C. T., Yang, W. T., and Parr, R. G.: Development of the Colle-Salvetti correlation-energy formula into a functional of the electron-density, Phys. Rev. B, 37, 785-789, 10.1103/PhysRevB.37.785, 1988.

Li, H., Riva, M., Rantala, P., Heikkinen, L., Daellenbach, K., Krechmer, J. E., Flaud, P. M., Worsnop, D., Kulmala, M., Villenave, E., Perraudin, E., Ehn, M., and Bianchi, F.: Terpenes and their oxidation products in the French Landes forest: insights from Vocus PTR-TOF measurements, Atmos. Chem. Phys., 20, 1941-1959, 10.5194/acp-20-1941-2020, 2020.

Li, H., Canagaratna, M. R., Riva, M., Rantala, P., Zhang, Y., Thomas, S., Heikkinen, L., Flaud, P. M., Villenave, E., Perraudin, E., Worsnop, D., Kulmala, M., Ehn, M., and Bianchi, F.: Atmospheric organic vapors in two European pine forests measured by a Vocus PTR-TOF: insights into monoterpene and sesquiterpene oxidation processes, Atmos. Chem. Phys., 21, 4123-4147, 10.5194/acp-21-4123-2021, 2021.

Lopez-Hilfiker, F. D., Pospisilova, V., Huang, W., Kalberer, M., Mohr, C., Stefenelli, G., Thornton, J. A., Baltensperger, U., Prevot, A. S. H., and Slowik, J. G.: An extractive electrospray ionization time-of-flight mass spectrometer (EESI-TOF) for online measurement of atmospheric aerosol particles, Atmos. Meas. Tech., 12, 4867-4886, 10.5194/amt-12-4867-2019, 2019.

Mohr, C., Thornton, J. A., Heitto, A., Lopez-Hilfiker, F. D., Lutz, A., Riipinen, I., Hong, J., Donahue, N. M., Hallquist, M., Petäjä, T., Kulmala, M., and Yli-Juuti, T.: Molecular identification of organic vapors driving atmospheric nanoparticle growth, Nature Communications, 10, 4442, 10.1038/s41467-019-12473-2, 2019.

Møller, K. H., Otkjaer, R. V., Hyttinen, N., Kurten, T., and Kjaergaard, H. G.: Cost-Effective Implementation of Multiconformer Transition State Theory for Peroxy Radical Hydrogen Shift Reactions, J. Phys. Chem. A, 120, 10072-10087, 10.1021/acs.jpca.6b09370, 2016.

Pagonis, D., Sekimoto, K., and de Gouw, J.: A Library of Proton-Transfer Reactions of H3O+ Ions Used for Trace Gas Detection, Journal of The American Society for Mass Spectrometry, 30, 1330-1335, 10.1007/s13361-019-02209-3, 2019.

Peräkylä, O., Riva, M., Heikkinen, L., Quéléver, L., Roldin, P., and Ehn, M.: Experimental investigation into the volatilities of highly oxygenated organic molecules (HOMs), Atmos. Chem. Phys., 20, 649-669, 10.5194/acp-20-649-2020, 2020.

Rap, A., Scott, C. E., Spracklen, D. V., Bellouin, N., Forster, P. M., Carslaw, K. S., Schmidt, A., and Mann, G.: Natural aerosol direct and indirect radiative effects, Geophys Res Lett, 40, 3297-3301, https://doi.org/10.1002/grl.50441, 2013.

Rissanen, M. P., Kurtén, T., Sipilä, M., Thornton, J. A., Kangasluoma, J., Sarnela, N., Junninen, H., Jørgensen, S., Schallhart, S., Kajos, M. K., Taipale, R., Springer, M., Mentel, T. F., Ruuskanen, T., Petäjä, T., Worsnop, D. R., Kjaergaard, H. G., and Ehn, M.: The Formation of Highly Oxidized Multifunctional Products in the Ozonolysis of Cyclohexene, Journal of the American Chemical Society, 136, 15596-15606, 10.1021/ja507146s, 2014.

Riva, M., Rantala, P., Krechmer, J. E., Peräkylä, O., Zhang, Y., Heikkinen, L., Garmash, O., Yan, C., Kulmala, M., Worsnop, D., and Ehn, M.: Evaluating the performance of five different chemical ionization techniques for detecting gaseous oxygenated organic species, Atmos. Meas. Tech., 12, 2403-2421, 10.5194/amt-12-2403-2019, 2019.

Schalley, C. A., Dieterle, M., Schröder, D., Schwarz, H., and Uggerud, E.: On the cleavage of the peroxide O O bond in methyl hydroperoxide and dimethyl peroxide upon protonation, International Journal of Mass Spectrometry and Ion Processes, 163, 101-119, https://doi.org/10.1016/S0168-1176(97)00001-3, 1997.

Schervish, M., and Donahue, N. M.: Peroxy radical chemistry and the volatility basis set, Atmos. Chem. Phys., 20, 1183-1199, 10.5194/acp-20-1183-2020, 2020.

Schreckenbach, S. A., Anderson, J. S. M., Koopman, J., Grimme, S., Simpson, M. J., and Jobst, K. J.: Predicting the Mass Spectra of Environmental Pollutants Using Computational Chemistry: A Case Study and Critical Evaluation, J Am Soc Mass Spectrom, 32, 1508-1518, 10.1021/jasms.1c00078, 2021.

Sindelarova, K., Granier, C., Bouarar, I., Guenther, A., Tilmes, S., Stavrakou, T., Müller, J. F., Kuhn, U., Stefani, P., and Knorr, W.: Global data set of biogenic VOC emissions calculated by the MEGAN model over the last 30 years, Atmos. Chem. Phys., 14, 9317-9341, 10.5194/acp-14-9317-2014, 2014.

Swanton, D. J., Marsden, D. C. J., and Radom, L.: Theoretical study of the structure and unimolecular decomposition pathways of ethyloxonium, [CH3CH2OH2]+, Organic Mass Spectrometry, 26, 227-234, https://doi.org/10.1002/oms.1210260409, 1991.

Tani, A., Hayward, S., and Hewitt, C. N.: Measurement of monoterpenes and related compounds by proton transfer reaction-mass spectrometry (PTR-MS), International Journal of Mass Spectrometry, 223-224, 561-578, https://doi.org/10.1016/S1387-3806(02)00880-1, 2003.

Tani, A., Hayward, S., Hansel, A., and Hewitt, C. N.: Effect of water vapour pressure on monoterpene measurements using proton transfer reaction-mass spectrometry (PTR-MS), International Journal of Mass Spectrometry, 239, 161-169, https://doi.org/10.1016/j.ijms.2004.07.020, 2004.

Theloke, J., and Friedrich, R.: Compilation of a database on the composition of anthropogenic VOC emissions for atmospheric modeling in Europe, Atmos Environ, 41, 4148-4160, https://doi.org/10.1016/j.atmosenv.2006.12.026, 2007.

Tomaz, S., Wang, D., Zabalegui, N., Li, D., Lamkaddam, H., Bachmeier, F., Vogel, A., Monge, M. E., Perrier, S., Baltensperger, U., George, C., Rissanen, M., Ehn, M., El Haddad, I., and Riva, M.: Structures and reactivity of peroxy radicals and dimeric products revealed by online tandem mass spectrometry, Nature Communications, 12, 300, 10.1038/s41467-020-20532-2, 2021.

Valiev, R. R., Hasan, G., Salo, V.-T., Kubečka, J., and Kurten, T.: Intersystem Crossings Drive Atmospheric Gas-Phase Dimer Formation, The Journal of Physical Chemistry A, 123, 6596-6604, 10.1021/acs.jpca.9b02559, 2019.

Werner, H. J., Knowles, P. J., Knizia, G., Manby, F. R., and Schutz, M.: Molpro: a general-purpose quantum chemistry program package, Wiley Interdiscip. Rev.-Comput. Mol. Sci., 2, 242-253, 10.1002/wcms.82, 2012.

Yan, C., Nie, W., Äijälä, M., Rissanen, M. P., Canagaratna, M. R., Massoli, P., Junninen, H., Jokinen, T., Sarnela, N., Häme, S. A. K., Schobesberger, S., Canonaco, F., Yao, L., Prévôt, A. S. H., Petäjä, T., Kulmala, M., Sipilä, M., Worsnop, D. R., and Ehn, M.: Source characterization of highly oxidized multifunctional compounds in a boreal forest environment using positive matrix factorization, Atmos. Chem. Phys., 16, 12715-12731, 10.5194/acp-16-12715-2016, 2016.

Ying, Q., and Krishnan, A.: Source contributions of volatile organic compounds to ozone formation in southeast Texas, Journal of Geophysical Research: Atmospheres, 115, https://doi.org/10.1029/2010JD013931, 2010.

Yuan, B., Koss, A. R., Warneke, C., Coggon, M., Sekimoto, K., and de Gouw, J. A.: Proton-Transfer-Reaction Mass Spectrometry: Applications in Atmospheric Sciences, Chem Rev, 117, 13187-13229, 2017.

Zhao, Y., Thornton, J. A., and Pye, H. O. T.: Quantitative constraints on autoxidation and dimer formation from direct probing of monoterpene-derived peroxy radical chemistry, Proceedings of the National Academy of Sciences, 115, 12142, 10.1073/pnas.1812147115, 2018.

Supplement of

Fragmentation inside PTR-based mass spectrometers limits the detection of ROOR and ROOH peroxides

Haiyan Li[1,2,†], Thomas Golin Almeida[3,†], Yuanyuan Luo[2], Jian Zhao[2], Brett B. Palm[4], Christopher Daub[3], Wei Huang[2], Claudia Mohr[5], Jordan E. Krechmer[6], Theo Kurtén[3], Mikael Ehn[2]

[1]School of Civil and Environmental Engineering, Harbin Institute of Technology, Shenzhen, 518055
[2]Institute for Atmospheric and Earth System Research / Physics, Faculty of Science, University of Helsinki, Helsinki, 00014, Finland
[3]Department of Chemistry, University of Helsinki, Helsinki, 00014, Finland
[4]Department of Atmospheric Science, University of Washington Seattle, Washington, WA, 98195, USA
[5]Department of Environmental Science, Stockholm University, 11418, Stockholm, Sweden
[6]Aerodyne Research, Inc., Billerica, MA, 01821, USA
†These authors contributed equally to this work.

Correspondence to: Haiyan Li (lihaiyan2021@hit.edu.cn), Mikael Ehn (mikael.ehn@helsinki.fi), Theo Kurtén (theo.kurten@helsinki.fi)

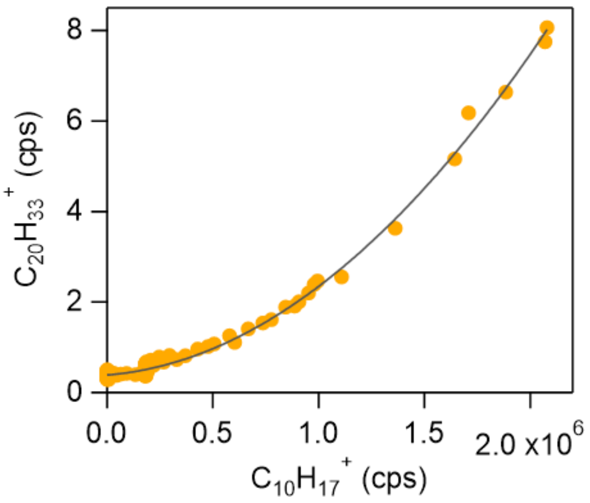

Figure S1. Correlation plot of $C_{10}H_{17}^+$ and the secondary ion cluster $C_{20}H_{33}^+$.

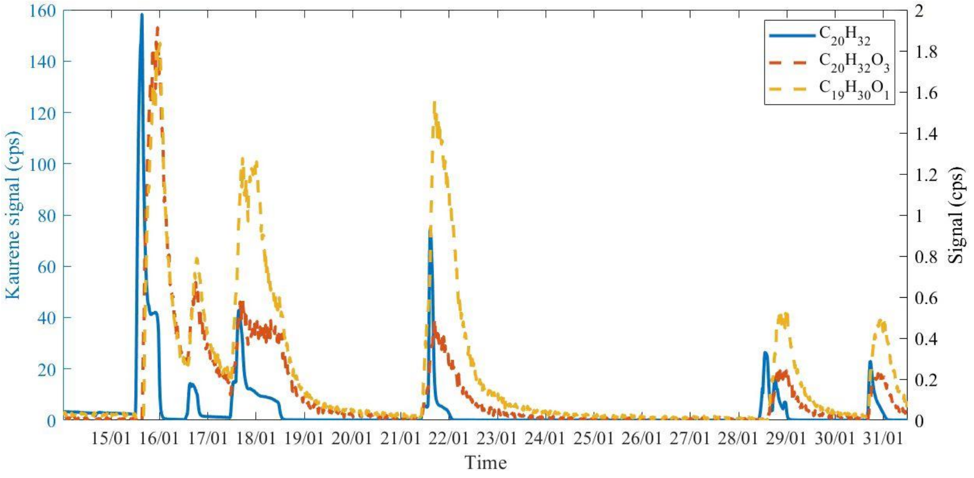

Figure S2. Time series of kaurene ($C_{20}H_{32}$) and its oxidation products $C_{19}H_{30}O$ and $C_{20}H_{32}O_3$ during the kaurene oxidation experiment.

S1 MESMER simulations.

Once the PES of each model ROOR and ROOH system was obtained, the time-dependent species distribution profile was estimated with MESMER (Master Equation Solver for Multi-Energy Well Reactions) version 6.0 (Glowacki et al., 2012). Together with zero-point corrected energies, vibrational frequencies and rotational constants for each stationary point were used as input. Since the investigated reactions happen in low pressures, and are preceded by an exothermic protonation step (Rp), kinetic and collisional relaxation time scales may be of similar magnitude. In such cases, Rice-Ramsperger-Kassel-Marcus (RRKM) th—eory offers a more appropriate treatment, and was accordingly used to model all isomerization steps in the master equation. The imaginary frequency of each transition state (mode associated with the reaction motion), was provided for calculation of the

Eckart tunnelling factor (Eckart, 1930).~~[13]~~ Irreversible dissociation steps were assumed to be barrierless, and were treated with the reverse Inverse Laplace Transformation (ILT) method. The Arrhenius pre-exponential factor was estimated according to a parameterized procedure for obtaining ion-dipole collision rates reported by (Su and Chesnavich, 1982), giving values in the range of 1~4 x 10^{-9} cm^3 $molecule^{-1}$ s^{-1}. A modified Arrhenius parameter (n^{∞}) value of 0.01 was used. The protonation step could not be modelled explicitly, because the treatment of bimolecular exchange reactions in MESMER requires a transition state, which was not found. Thus, the initial charged species (RH^+) was modelled as having emerged from a barrierless dissociation reaction, $A(E_{ex}) \rightarrow RH^+ + H_2O$, where E_{ex} is the excess energy in reactant A, which was assumed to be equal to the zero-point corrected energy of reaction R1p (ΔE_{zp}). This could be done by using the Prior method for the initial distribution of states, where the E_{ex} is shared between the dissociation products according to a probability distribution. The probability that RH^+ emerges from the reaction with energy E is given as described in MESMER's manual:

$$p_{ROORH^+}(E, E_{ex}) = \frac{\rho_{ROORH^+}(E)\,.\,[\rho_t * \rho_{H_2O}](E_{ex} - E)}{[\rho_{ROORH^+} * \rho_t * \rho_{H_2O}](E_{ex})}$$

Where $\rho_{ROORH^+}(E)$ and ρ_{H_2O} are the rovibrational density of states of RH^+ and H_2O respectively, and ρ_t is the relative translational density of states of RH^+ and H_2O. The expression $[x * y](E)$ is a convolution:

$$[x * y](E) = \int_0^E x(E - \tau)y(\tau)d\tau$$

The exponential down model was employed for collisional energy transfer, and the Lennard-Jones potential for estimating collisional frequency. The employed parameters were obtained by fitting MESMER's simulated collision frequency and collisional relaxation rate to the results from Molecular Dynamics calculations, as described in the next section. The values used for the smaller systems (< 39 atoms) were: $\langle \Delta E_{down} \rangle$ = 145 cm^{-1}; ε_{LJ} = 200 K; σ_{LJ} = 10 Å. For the larger systems the values $\langle \Delta E_{down} \rangle$ = 185 cm^{-1}; ε_{LJ} = 550 K; σ_{LJ} = 11 Å were used. N_2 was assigned as bath gas, with Lennard-Jones parameter values ε_{LJ} = 91.85 K and σ_{LJ} = 3.919 Å. Energy grains were set to span values up to 20 k_BT above the highest stationary point and their size was set to 30 cm^{-1}.

S2 Estimation of thermalization rates with Molecular Dynamics.

S2.1 Introduction

During many atmospheric reactions of interest, the product state has a lower total energy than the reactant state. As a result, the initial temperature of the product(s) will be significantly higher than the reactant(s). In the atmosphere, collisions with atmospheric gases (N_2, O_2, etc.) will thermalize the products, bringing the temperature into equilibrium. However, quantifying how this process works is not trivial. Models for the energy transfer processes involved in molecular collisions have certainly been developed (Michael et al., 2002; Miller and Klippenstein, 2006; Pilling and Robertson, 2003; Senosiain et al., 2006), and are included in master equation solving software such as MESMER (Glowacki et al., 2012) used to describe complex gas-phase reaction kinetics. However, these models may be somewhat limited; in particular, they have been developed for and demonstrated to work on rather small molecules and it is unknown how well they may be applied to describe thermalization in larger gas-phase molecules. In this work, we use classical molecular dynamics simulations with empirical force fields to model the thermalization of some of the studied ROOR' compounds as they undergo collisions in a nitrogen atmosphere. Then, we demonstrate how to use our results to obtain the parameters ~~improve~~ for the stochastic models for thermalization used in MESMER. It is worth noting that the values for these parameters offered by the software as a default should be used with caution, as they may lead to significant underestimation of ~~In particular, it is apparent that the models used by MESMER significantly underestimate~~ the thermalization rate of larger molecules~~e collision rate between nitrogen gas and a large gas-phase molecule, and therefore when using the default parameters the rate of thermalization is in turn underestimated~~.

S2.2 Potential Models

We used LAMMPS (Plimpton, 1995) to run classical molecular dynamics simulations. OPLS-AA (Jorgensen et al., 1996; Jorgensen and Tirado-Rives, 2005; Kaminski et al., 2001) served as a baseline forcefield for describing a large atmospheric molecule. We used the LigParGen online server (Dodda et al., 2017) to automatically generate a LAMMPS data file for each molecule. In this work, we focus in particular on some molecules which contain peroxide bonds (ROOR'). Since peroxides are not specifically included in the OPLS-AA parameter set we incorporate Lennard-Jones potential parameters, partial charges, bond, and angular terms derived elsewhere for simulations of peroxide and peroxyl groups (Garrec et al., 2014). To model nitrogen molecules, we use a simple model for diatomics, consisting of two Lennard-Jones atoms linked by a rigid bond. No electrostatic interactions are included. The original source for the model is ~~Ref. 12~~ Cheung and Powles (1975). However, we copied the parameters from a later paper (Lee and Kim, 2014), which mistakenly switched the value of ε between O_2 and N_2. As a result, in the model we adopted we had $\sigma_N = 3.31$ Å, $\varepsilon_N/k_B = 61.6$ K, with a bond length of 1.1 Å. We did test simulations using the correct value of $\varepsilon_N/k_B = 37.3$ K and found no significant difference in the results. Since the energetics of dilute gases are dominated by kinetic energy, it is not surprising that small differences in the potential model would not have a noticeable effect on our findings. It is also worth noting that both the OPLS-AA parameters, and the nitrogen parameters, were derived for simulations of molecules in aqueous environments and liquid nitrogen, respectively, and so it is worth considering whether they can be applied to a gas phase simulation. Recent work has shown that simulations of protein ions in the gas phase are more or less accurate using parameter sets designed for solvated biomolecules, and rather large reductions in the partial charges are needed to cause appreciable effects (Lee et al., 2019). As far as the nitrogen model is concerned, it has been used previously for simulations of gas phase nitrogen and has been shown to perform well (Lee and Kim, 2014; Wang et al., 2020).

S2.3 Simulation methodology

Our initial simulation box consisted of one analyte molecule in the center of the box, surrounded by randomly placed nitrogen molecules. The cubic box length L = 400 Å, and 1540 N_2 molecules were added to give a pressure P = 1 atm. Other simulations were done with 385 gas molecules, P = 0.25 atm. We consistently used a timestep of 0.5 fs throughout the work. The SHAKE algorithm was used to hold the N_2 bond length constant, as well as any OH bonds in the analyte molecules. Systems were equilibrated in the NVT ensemble for 5 ns using two different Nose-Hoover thermostats to separately maintain the temperature of the analyte molecule and the N_2 gas. The initial temperature of the analyte T_{molec} was set to 800 K, with the nitrogen temperature T_{gas} set to 300 K. After equilibration, the thermostats were removed and the remainder of the simulation proceeded using NVE integration. As the simulation proceeded collisions between gas and analyte served to bring the temperature of the gas and the analyte closer together. Simulations were run long enough so that the overall temperature became uniform, typically 25 to 50 ns.

S2.4 Results and discussion

In Figure S3 we plot $\Delta T(t) = T_{molec} - T_{gas}$ as a function of the simulation time. There is considerable variation in individual simulation runs, so we average over several simulations to reduce the statistical noise.

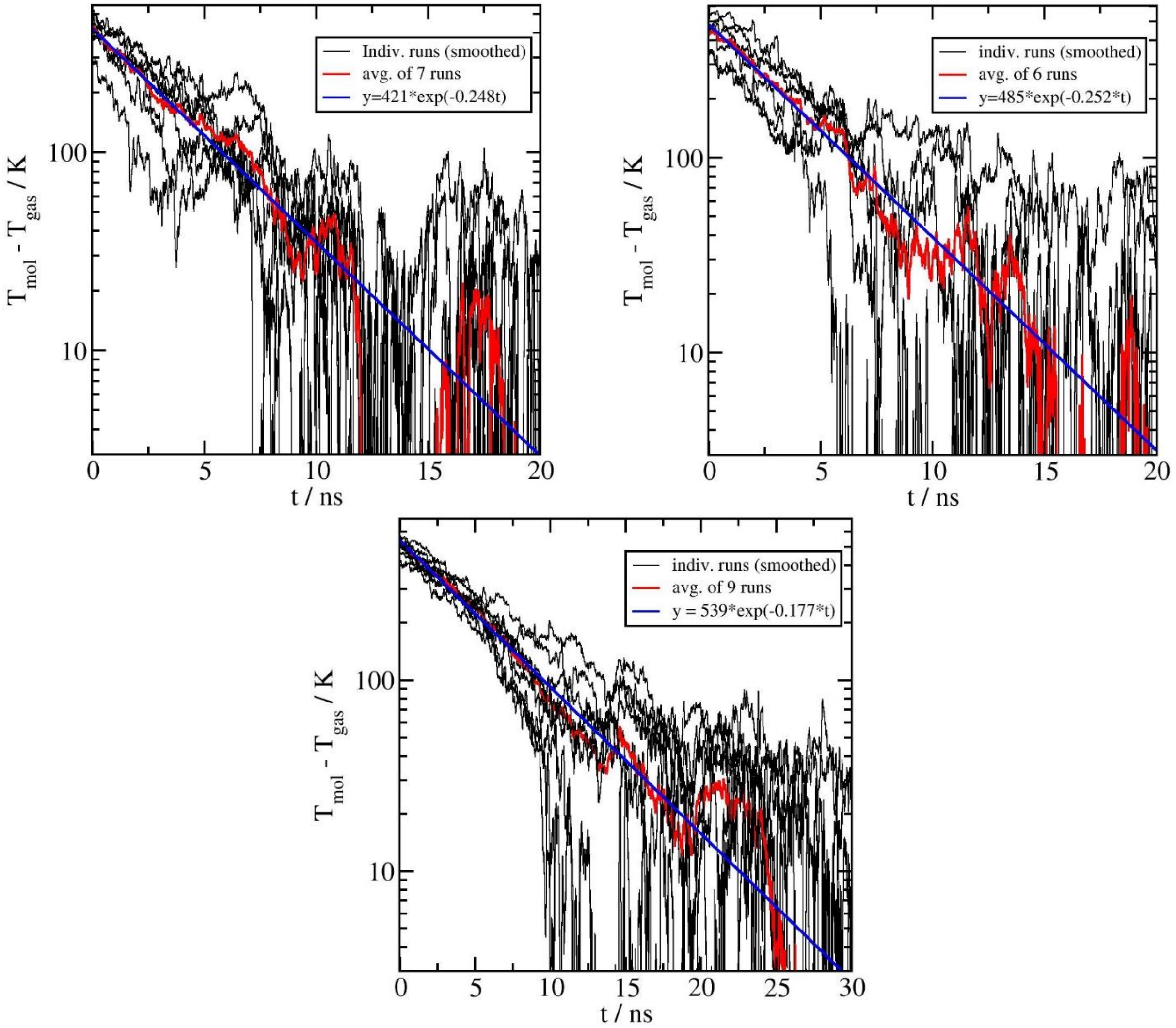

Figure S3: Temperature difference between analyte molecule and surrounding gas for $(EtOOEt)H^+$ (top left), and isomer M3 of the decomposition mechanism of EtOOEt (top right) and ROOR derived from OH oxidation of cyclohexene (bottom). Individual simulation runs are shown in thin black lines, with the average over all simulations in red. The blue line is a fit to an exponential function $\Delta T(t) = Ae^{-Bt}$, with the numerical values of the fit parameters given in the legend.

We find that a single exponential function of the form:

$$\Delta T(t) = Ae^{-Bt} \tag{S1}$$

fits the temperature difference well in all cases we have studied. The inverse of the constant B in Equation S1 can be interpreted as a characteristic time. For the systems we have studied, and with a gas pressure of 1 atm, this time is on the order of 1 to 10 ns; however, there is considerable variation for different molecules. In the examples we focus on here, we note that the cyclohexene derived ROOR' takes longer to reach the same temperature as the gas compared to the two ethyl peroxide dimers (ca. 5.5 ns vs. 4 ns). By post-processing the trajectories, we obtained more information about the collision events. We define a collision starting if either a nitrogen atom gets closer than 4 Å to one of the atoms in the analyte molecule, and ending when both nitrogen atoms are further away than 4 Å from all of the atoms in the analyte. One complication is the possibility of multiple gas molecules colliding simultaneously; to mitigate against this rare occurrence we ran more simulations with a reduced gas pressure of 0.25 atm. This analysis allows us to compute the gas collision frequency f_{coll}.

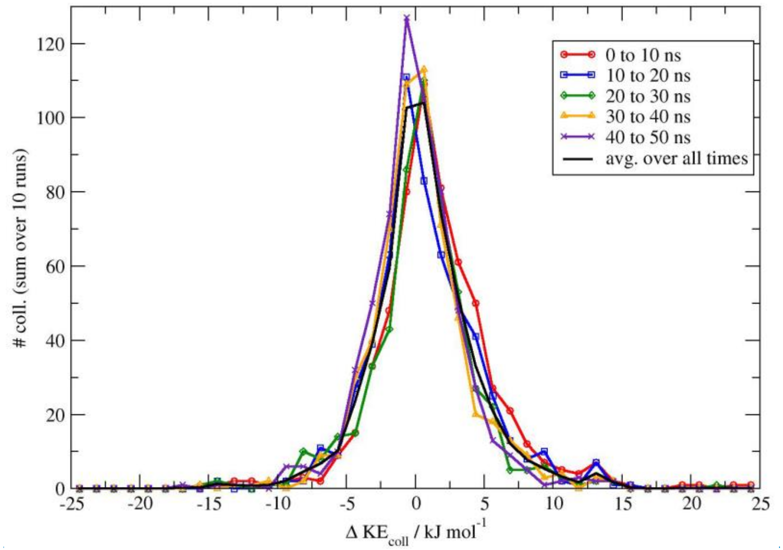

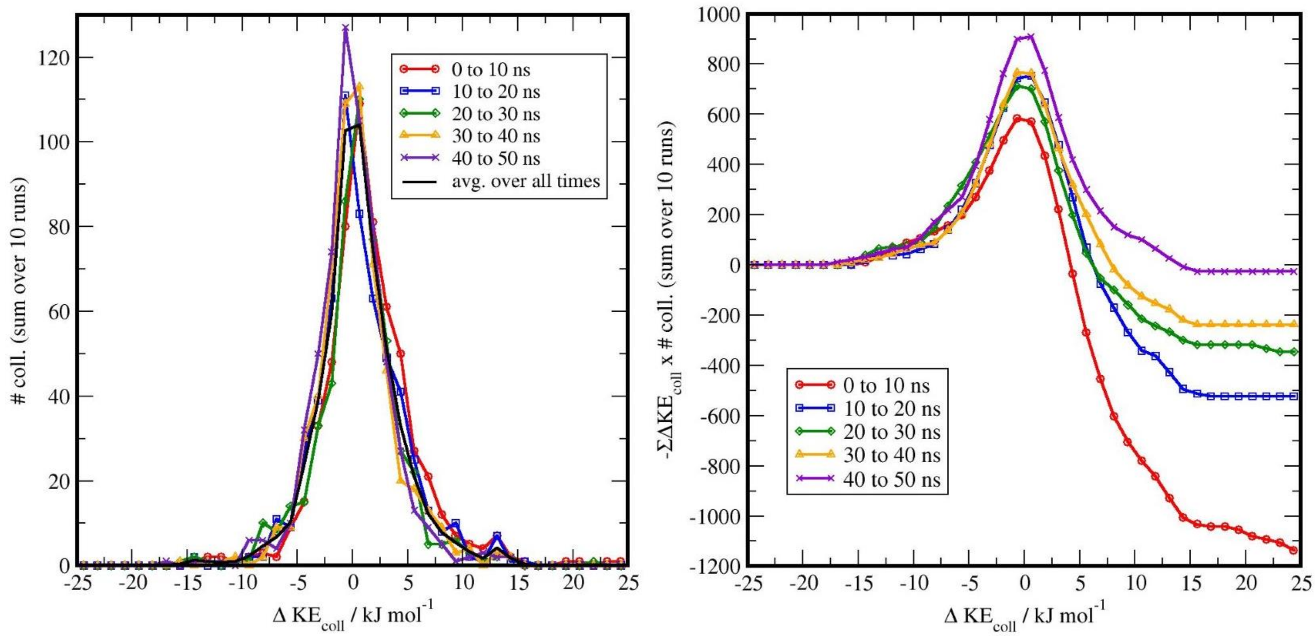

Figure S4: Left: Histogram of the change in the kinetic energy of the colliding gas molecule ΔKE_{coll} during 10~~9~~ independent simulations with the $(EtOOEt)H^+$ molecule. Right: Cumulative sum of the change in kinetic energy of N_2 before/after each collision ($\sum \Delta KE_{coll}$), multiplied by the number of collisions of that energy. The quantity is multiplied by -1 so that the sum over all collision energies represents the total energy lost by the analyte molecule during each time interval, over the course of 10 individual simulations. The density of N_2 is 0.25 atm.

Table S1: Summary table. $1/B$ is the characteristic time decay constant in Equation 1 from the average of several simulations with 1 atm gas pressure. f_{coll} and $\langle KE_{coll}\rangle$ are the average gas collision rate and kinetic energy transfer from several simulations with 0.25 atm, respectively.

Analyte	$1/B$ (ns)	f_{coll} (ns^{-1})	$\langle KE_{coll}\rangle$ $(kcal.mol^{-1})$
M1 (EtOOEt)	4.0	5.98	0.715
M3 (EtOOEt)	4.0	6.19	0.519
M3 (Cyclohexene + OH)	5.6	7.85	0.996

Another quantity of interest is the energy transfer per collision. We compute the kinetic energy of the gas molecule as an average, using velocities spanning from 3.0 ps to 2.5 ps before/after each collision event. Then we can compute the change in kinetic energy $\Delta KE_{coll} = KE_{after} - KE_{before}$. There is a large variation in the ΔKE_{coll} measured in each collision. In Figure S4 we show a histogram of the ΔKE_{coll} for all collisions during a series of 10~~9~~ simulation runs. We see that the probability of collisions which lower the KE of the colliding gas molecule is nearly the same as those which raise the KE. The overall temperature equilibration must therefore arise from the relatively small asymmetry in this histogram, which we see from Figure S4 becomes more symmetric as the simulation proceeds and the temperatures of the gas and analyte become closer (Tardy and Rabinovitch, 1977). In Table S1 we summarize the values of the temperature decay time constant 1/B, the gas collision frequency f_{coll} and the average kinetic energy change per collision $\langle KE_{coll}\rangle$ for three different molecules of interest. These quantities will be used in comparison with the MESMER stochastic models to improve the calculations of reaction rates in MESMER.

S2.5~~4~~ Fitting MESMER parameters

Table S2: Selected Lennard-Jones parameters and resulting collision frequency f_{coll} and fitted ΔE_{down} value for MESMER simulations at 1 atm.

Species	ε/k_B (K)	σ (Å)	f_{coll} (ns^{-1})	ΔE_{down} $(kcal.mol^{-1})$
M1 (EtOOEt)	200	10	23.2	0.415
M3 (Cyclohexene + OH)	550	11	30.0	0.529

A series of MESMER simulations were done with $EtOOEtH^+$ and the isomer M3 of the ROOR derived from cyclohexene + OH oxidation, varying Lennard-Jones parameters ε and σ in order to find the combination that yields a value of f_{coll} at 1 atm that agrees with results from MD calculations. For the smaller molecule, these values were $\varepsilon/k_B = 200$ K and σ = 10 Å, while for the larger species the selected values were $\varepsilon/k_B = 550$ K and σ = 11 Å (Table S2). The resulting f_{coll} values at 1 atm were 23.2 ns^{-1} and 30.0 ns^{-1} for M1 (EtOOEt) and M3 (Cyclohexene + OH) respectively, being very close to the MD values, assuming that the collision frequency is linearly dependent to pressure. The selected parameter values for M1 (EtOOEt)~~, in special σ, are much higher than those offered by MESMER as default~~deviate significantly from values empirically fitted for thermalization of hexane ($\varepsilon/k_B = 343$ K and σ = 6.25 Å) (Hippler et al., 1983), a similarly sized molecule, ~~($\varepsilon/k_B = 50$ K and σ = 5 Å)~~ and may represent an unrealistic description of the Lennard-Jones potential well. However, the ~~high~~ obtained values were ~~needed~~ selected to yield a f_{coll} that agrees with the MD results, and do not interfere with any other function in MESMER's model. Having fixed those parameters, another series of MESMER simulations were done where the investigated species starts at a temperature of 800 K, varying the exponential-down model parameter $\langle \Delta E_{down} \rangle$. The obtained time-dependent internal energy profiles were then compared to the results from MD calculations. The $\langle \Delta E_{down} \rangle$ value yielding the thermalization curve with closest agreement with results from MD calculations, shown in Table S2 and Figure S5, was selected for use in this study.

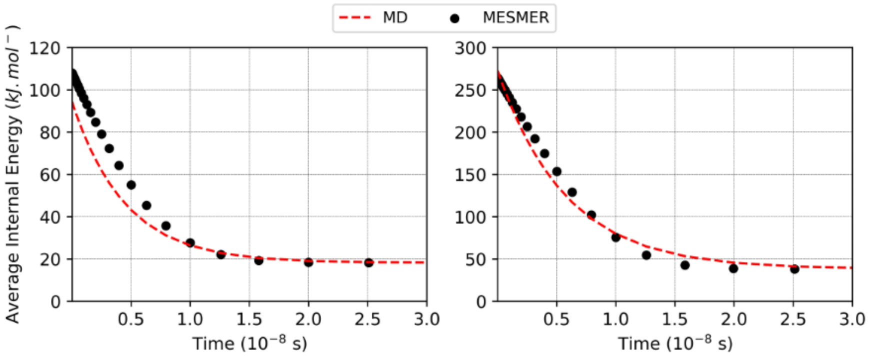

Figure S5. Collisional relaxation curves obtained from MD and MESMER calculations for $EtOOHEt^+$ (a) and isomer M3 of the cyclohexene + OH oxidation derived ROOR (b), at 298.15 K and 1 atm. In both methods the starting temperature of the analyte is 800 K. Fitted Lennard-Jones parameters and exponential-down values are: a) $\langle \Delta E_{down} \rangle$ = 145 cm^{-1}; ε_{LJ} = 200 K; σ_{LJ} = 10 Å; b) $\langle \Delta E_{down} \rangle$ = 185 cm^{-1}; ε_{LJ} = 550 K; σ_{LJ} = 11 Å.

S3 Reaction Mechanism and Energetics.

The general mechanism for fragmentation of ROOR' and ROOH are shown in Scheme 2 and 3 respectively. The calculated Potential Energy Surfaces are depicted in Figures S6-13. Important values for structure and reactivity analysis, such as protonation energies, initial step barrier heights and direct dissociation energies, are shown in Table S3.

S3.1 Model ROOR.

The calculations revealed that the rate-determining step, i.e. the step with the highest barrier on the most favourable reaction pathway, is **R1a** for the MeOOMe system and **R1c** for HOEtOOMe and O=EtOOMe. For the EtOOEt and iPrOOiPr systems, these two steps share a very similar reaction barrier height, and both should be rate-determining. **R1a** involves the cleavage of the peroxy O-O bond with a concerted H migration to the unprotonated peroxy O from its adjacent carbon (1,2 shift), leading to the formation of a proton-bridged alcohol-aldehyde/ketone (**M2**). In step **R1c**, the O-O bond cleavage occurs alongside the 1,2 shift of an organic substituent instead. In most cases, the two fragments formed, an alcohol and a carboxonium ion, rapidly undergo addition to form a protonated acetal/ketal (**M6**). IRC calculations indicate that with O=EtOOMe, this addition does not occur, and **R1c** yields a product complex. Nevertheless, the constituting fragments of the product from **R1c**, either covalently bound or complexed, may suffer barrierless dissociation into **P6**. A third initial step (**R1b**) was found, where the peroxy O-O bond cleavage occurs with concerted H_2 elimination from the C(OO)C carbon atoms, via a ring-like transition state. This channel leads to the formation of a proton-bridged pair of aldehydes/ketones (**P4**), but it was not found to be competitive. The key branching point in the reaction mechanism following **R1a** appears to be the not-so-loosely bound species **M2**. Reaction channels available for **M2** include: nucleophilic attack on the carbonyl C by the alcohol O (**R2a**), producing a protonated hemiacetal/hemiketal (**M3**); H_2 elimination (**R2b**), producing the proton-bridged pair of aldehydes/ketones (**P4**); barrierless dissociation (**R2c** or **R2d**) into alcohol + protonated aldehyde/ketone (**P1**) or protonated alcohol + aldehyde/ketone (**P2**). Species **M3** may further react by a 1,3-H transfer to the hydroxyl O, concerted with a C-OH bond cleavage (**R3a**), yielding a H_2O:carboxonium ion complex (**M4**). Complex **M4** fragments may in turn fly apart into **P3** + H_2O (**R4b**), or react with each other producing **P2**

(R4a). The proton-bridged pair of aldehydes/ketones (**P4**) can also dissociate (**R5**) into its constituting fragments (**P5**). Three channels involving direct dissociation of the initial reactant without rearrangement are available, but none was observed to be competitive for the model ROOR' systems: Heterolytic C-O bond cleavage yielding a hydroperoxide R'OOH and the corresponding carbocation R^+ (**R9**); Homolytic O-O bond cleavage yielding an alkoxy radical $R'O^{\bullet}$ and an alcohol radical cation $ROH^{\bullet+}$ (**R10**); and a homolytic analogue of **R9**, yielding a hydroperoxide radical cation $R'OOH^{\bullet+}$ and a carbon centered radical $R^{\bullet}$ (**R11**).

Table S3. Protonation energy, initial step barrier heights and direct dissociation energies calculated at the RHF-RCCSD(T)-F12a/VDZ-F12 // ωB97XD/aug-cc-pVTZ level of theory for ROOR and ROOH decomposition. All values correspond to zero-point corrected energies, given in kcal mol^{-1}, relative to the lowest energy protonation isomer of the initial charged species. Species structures are given in Scheme 2 and 3.

(ROOR')H$^+$	**ROOR' + H$_3$O$^+$ – H$_2$O**	**TS 1a**	**TS 1b**	**TS 1c**	**TS 1d**	**P9**	**P10**
Me-OO**H**-Me$^+$	15.38	21.06	23.35	---	---	72.26	49.97
Et-OO**H**-Et$^+$	23.40	15.43	20.28	15.35	---	43.44	46.07
iPr-OO**H**-iPr$^+$	28.54	12.25	22.41	12.26	---	35.03	45.94
HOEt-OO**H**-Me$^+$	32.88	29.54	---	22.00	---	43.83	68.15
HO=Et-OO-Me$^+$	27.03	36.52	---	21.34	---	61.16	38.84
(Cyclohexene + OH)	52.63	28.26	---	26.35	---	37.18	33.56
(Cyclohexene + O$_3$)	56.03	35.34	---	26.31	20.40	30.00	34.83
(ROOH)H$^+$							
Me-OO**H**-H$^+$	4.29	10.95	---	---	---	---	---
Me-**H**OO-H$^+$	8.32	---	---	---	---	64.75	47.82
Et-OO**H**-H$^+$	7.58	4.52	---	3.08	---	---	---
Et-**H**OO-H$^+$	14.15	---	---	---	---	33.97	42.01
iPr-OO**H**-H$^+$	10.97	2.07	---	1.21	---	---	---
iPr-**H**OO-H$^+$	18.97	---	---	---	---	24.53	39.28
tBut-OO**H**-H$^+$	13.62	---	---	0.12	---	---	---
tBut-**H**OO-H$^+$	23.34	---	---	---	---	16.61	37.43
H$_2$OEt-OO-H$^+$	27.04	25.18	---	22.25	---	37.52	40.02
HO=Et-OO-H$^+$	21.31	32.47	---	25.79	---	81.63	38.68
(Cyclohexene + OH)	36.56	22.24	---	16.23	---	19.02	24.04
(Cyclohexene + O$_3$)	42.99	31.86	---	22.47	25.14	22.76	32.76

Considering the alky-substituted ROOR' systems, faster fragmentation rates were observed with increasing degree of substitution (R = Me < R = Et < R = iPr). The reason behind this trend is an increasing exothermicity of protonation by H_3O^+ and decreasing barrier heights for rate-determining steps **R1a** and **R1c**. The first of these factors may be explained by the greater electronic density introduced into the peroxy oxygens by methyl groups via inductive effects, increasing the proton affinity of the peroxide. The second factor can be understood by examining the part of the molecule where a 1,2-migration occurs during steps **R1a** and **R1c** when, en route to the transition state, the α-carbon atom increasingly becomes electron-deficient and assumes a sp^2 character. The C-H σ-bonds present in an adjacent methyl group may interact with this C atom's partially empty p-orbital, stabilizing the transition state by hyperconjugation. Thus, in comparison to the MeOOMe system, the presence of one methyl group (EtOOEt) lowers the **R1a** reaction barrier by 5.7 kcal mol^{-1}; and a second methyl group (iPrOOiPr) lowers this barrier by an additional 3.1 kcal mol^{-1}. In reaction step **R1c**, the group undergoing 1,2-shift to the oxygen atom is one of these methyl groups, which cannot participate in hyperconjugative stabilization of the transition state. Yet within the same reacting system, steps **R1a** and **R1c** have very similar barrier heights. Additional insight into the energetics of these competing channels is brought by analysing the kinetics of Baeyer-Villiger reactions (Clayden et al., 2012). During the rearrangement, a part of the positive charge may be allocated on the group being transferred, and therefore groups that better accommodate this charge stabilize the transition state to a greater degree. The importance of such factor is evidenced by the dissociative character of the rearrangement in the transition states of **R1a** and **R1c**, where the shifting group sits closer to the C than to the O atom. Methyl cation is a better leaving group than H^+, and therefore as far as the migrating group is concerned, a 1,2-shift involving the former (**R1c**) is more favourable than with the latter **(R1a)**.

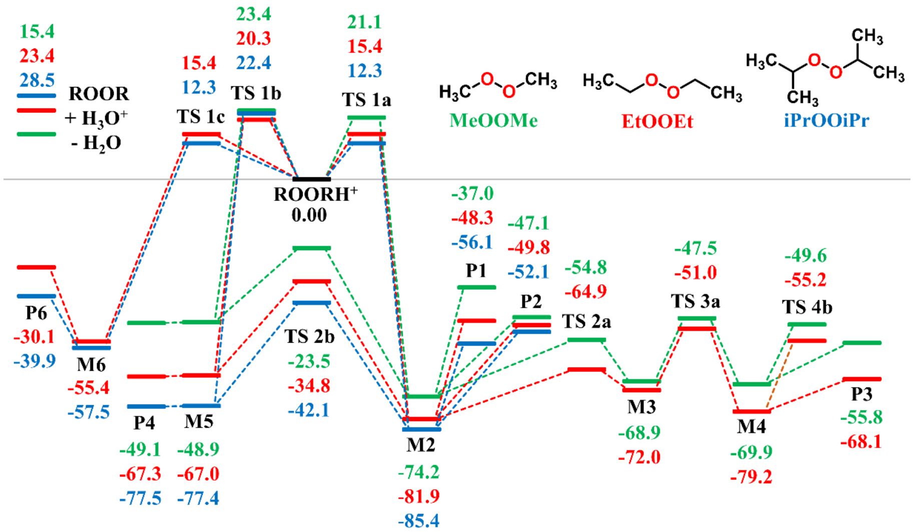

Figure S6. Potential energy surface calculated at the RHF-RCCSD(T)-F12a/VDZ-F12// ωB97XD/aug-cc-pVTZ level of theory, for decomposition of Me-OO-Me (green), Et-OO-Et (red) and iPr-OO-iPr (blue) following protonation in the gas phase. Molecular structures for stationary points are shown in Scheme 2. Values given are relative zero-point corrected energies in kcal ~~·~~mol^{-1}.

At the lower limit of excess energy, significant decomposition of MeOOMe occurs only after ~1 s, the major products being protonated methanol + formaldehyde (**P2**) and protonated formaldehyde + methanol (**P1**) with a branching ratio of 0.92 and 0.08 respectively. End products and respective branching ratios for decomposition of EtOOEt are **P6** (0.62), **P2** (0.31), **P1** (0.06) and **P3** (0.01); while those for iPrOOiPr are **P6** (0.55), **P2** (0.32) and **P1** (0.13). Species **M3** is not a stable minimum in the PES of iPrOOiPr, since geometry optimizations lead to a different structure. This result makes sense considering the high steric strain present in such a molecule. A transition state for **R2a** was also not found for iPrOOiPr, so this step and all those that would follow it are assumed to be unavailable for this ROOR. Observing the PES for the channels available for intermediate **M2**, shown in Figure S6, it would be expected that most of MeOOMe and EtOOEt reacting through **R1a** would subsequently follow **R4a**, the most energetically favourable dissociation route. However, reaction dynamics simulations revealed that **P3** is only a minor fragmentation product. The reason behind this result may be that, upon reaching **M2**, the reacting system accumulates considerable excess internal energy, enough to promote immediate dissociation into **P1** or **P2** before a significant fraction of species can further react to yield **M4** (Schalley et al., 1997).

As for the systems containing oxygenated substituents, HOEtOOMe and O=EtOOMe, relatively less fragmentation was observed within relevant time scales. At 1.023 mbar, ~68.2% of HOEtOOMe and ~24.6% of O=EtOOMe are left intact after 100 μs, the major fragmentation product being **P6** in both cases. As described in the beginning of this section, interconversion between the initial protonation isomers was found to be fast. Very low-lying transition states were found for steps **R0b** in the PES of HOEtOOMe, whereas no transition states were found for the O=EtOOMe counterparts. Thus, for the sake of analysis of the rate of decomposition of these two peroxides, all of their initial reaction step transition states can be assumed to be connected to their most stable protonation isomer, HOEtOO**H**Me$^+$ and **H**O=EtOOMe$^+$, shown in Figure S7. Both species have an intramolecular H-bond between a peroxy group's and the substituent's oxygen atom, in a six-member ring-like conformation. This factor grants extra stability to these protonation isomers, as seen by the larger exothermicity of reaction of the parent peroxides with H_3O^+, compared to EtOOEt (Table S3). Calculations with O=EtOO**H**Me$^+$ indicate that the most favourable conformation of this species is not a minimum in the PES, since the proton is transferred to the carbonyl-oxygen during geometry optimisation. By having the carbonyl as the protonation site, reactant **H**O=EtOOMe$^+$ is further stabiliz~~s~~ed by resonance. Higher energy protonation isomers HOEt**H**OOMe$^+$ and O=Et**H**OOMe$^+$ also make an intramolecular H-bond, but in a more rigid five-member ring-like conformation, which is weaker due to the less then optimal O---H-O angles. No such H-bond is present in the **R1c** and the two **R1a** transition states available in the PES of HOEtOOMe (Figure S7), which partly explains the higher barriers, and therefore the lower reaction rates. The same is true for the **R1c** and the lowest energy **R1a** transition state in the PES of O=EtOOMe. IRC calculation with the **TS1a** connected to isomer HOEtOO**H**Me$^+$ revealed that this reaction step would produce the protonated hemiacetal (**M3**) instead of **M2**, even though the latter is lower in energy.

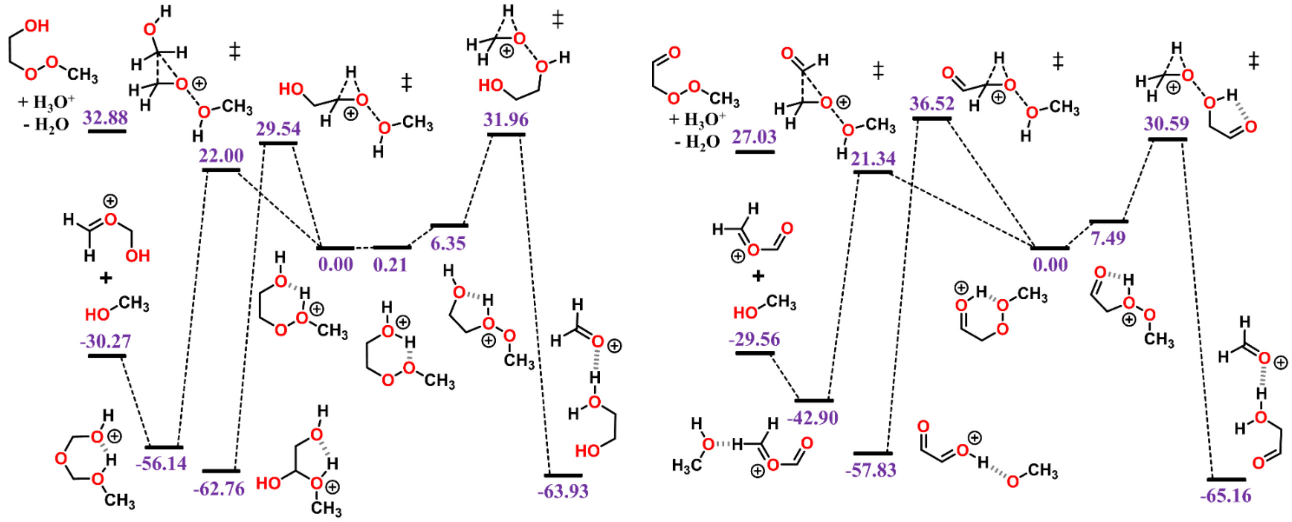

Figure S7. Potential energy surface calculated at the RHF-RCCSD(T)-F12a/VDZ-F12//ωB97XD/aug-cc-pVTZ level of theory for the initial steps in the decomposition of HOCH2CH2OOMe (left) and OCHCH2OOMe (right) following protonation in the gas phase. ~~Molecular structures carrying the double-dagger symbol ‡ are transition states.~~ Values given in purple are relative zero-point corrected energies in kcal ~~·~~mol^{-1}.

The absence of H-bonds in transition states described above results from a stereochemical constraint of such reactions (Clayden et al., 2012), where the migrating group has to be anti-periplanar to the leaving (alcohol) group. During the rearrangement, the electrons in the breaking C-C (or C-H) σ orbital gradually move into the empty O-O σ* orbital. Optimal overlap between these orbitals is achieved with an anti-periplanar conformation between the two involved moieties. Different to alkyl-substituted systems, HOEtOOMe and O=EtOOMe react only through the channel starting with **R1c**, as a result of the much lower reaction barrier of this step relative to **R1a** (Table S3). Due to resonance, both $-CH_2OH$ and -CHO can accommodate a partial positive charge better than a methyl group, thus stabilizing the **R1c** transition state to a greater degree when taking part in the 1,2-shift. However, $-CH_2OH$ is not as effective in stabilizing an adjacent carbocationic center, having C-H bonds available for hyperconjugation, but also an electron-withdrawing OH group. As a result, the **R1a** transition encountered by HOEtOO**H**Me$^+$ is not stabilized to the same extent as **R1c**. The -CHO group is moderately electron-withdrawing by induction, producing instead a destabilizing effect on the **R1a** transition state encountered by **H**O=EtOOMe$^+$, yielding the largest barrier for this step (36.5 kcal ~~-~~mol^{-1}) among the studied model ROOR' systems.

The reaction of protonated AcOOAc, which follows a different mechanism, is shown through its PES in Figure S8. Initial reaction with H_3O^+ can occur with protonation of a carbonyl-oxygen or a peroxyl-oxygen. Since a protonated carbonyl favors a planar geometry, the former may produce two isomers (**E** and **Z**), depending on which "side" of the functional group the proton is transferred to. However, the torsional barrier between the two isomers is relatively low (~11 kcal ~~-~~mol^{-1}) and interconversion occurs at time scales shorter than other reaction pathways. The peroxyl-oxygen protonated AcOOAc was not found to be a stable minimum, since geometry optimization leads instead to a dissociation product complex, where the fragments are an acylium ion (Ac$^+$) and peracetic acid (AcOOH). This result is similar to what was obtained for calculations with protonated acetic acid by Shi et al. (2015), where protonation at the hydroxyl-oxygen leads to a H_2O : acylium ion complex. The charged AcOOH:Ac$^+$ complex is however strongly bound, and reassociation with concerted H transfer to the carbonyl-oxygen has a very low barrier (1.37 kcal ~~-~~mol^{-1}), producing the more stable Z-isomer of the carbonyl-protonated AcOOAc. The only reaction pathway left to consider is a rearrangement available for the **E** and **Z** isomers, leading to a protonated acetic methylcarbonic anhydride (AMCAH$^+$). The barrier for this reaction is low compared to the energy released during protonation and the produced anhydride is stable. Reaction dynamics simulations revealed that after 100 μs, at 1.023 mbar and 298.15 K, about 18% of protonated AcOOAc is converted to AMCAH$^+$ and only ~1% yields the fragmentation products (AcOOH + Ac$^+$).

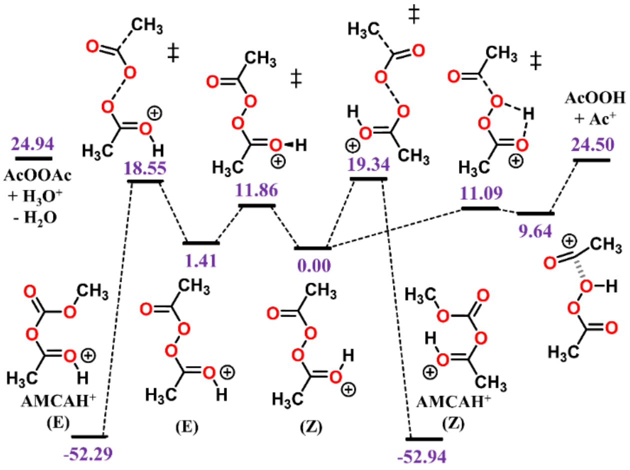

Figure S8. Potential energy surface calculated at the RHF-RCCSD(T)-F12a/VDZ-F12// ωB97XD/aug-cc-pVTZ level of theory for the reaction of AcOOAc following protonation in the gas phase. ~~Molecular structures carrying the double-dagger symbol ‡ are transition states.~~ Values given in purple are relative zero-point corrected energies in kcal ~~-~~mol^{-1}.

S3.2 Model ROOH.

For ROO**H**$_2^+$ the initial step with the lowest barrier is of the **R1a** type for R=Me and **R1c** type for R=Et, iPr or tBut, analogous to the ones found for ROOR, but in this case the molecule dissociates into a proton-bridged aldehyde/ketone : water complex (**M2**) or a carboxonium ion : water complex (**M6**). The trend in energetics for protonation exothermicity and initial step barrier height is the same as for the ROOR analogues, where the former increases and the latter decreases with larger substituents (R = Me < R = Et < R = iPr), likely due to the same factors discussed in the ROOR section. However, the energy released during protonation by H_3O^+ is considerably smaller for ROOH systems, which could reduce the proportion of molecules that react at non-thermal rates. On the other hand, the barrier heights for the (rate limiting) step **R1a** are also much lower for the alkyl-substituted

ROOH systems, meaning thermal reaction rates are faster. Given that any of the considered R groups have a greater electron-donating effect than a hydrogen, a ROOH system has a smaller proton affinity and its O-O bond is more polarized compared to a ROOR.

Reaction dynamics simulations for MeOO**H**$_2^+$ revealed that this species decomposes only at thermal rates across the pressure range considered here, which is evidenced by the single, pressure dependent decay curve (Figure 5). At 1.023 mbar, about ~17% of MeOO**H**$_2^+$ is decomposed after 100 μs, opposed to ~0% observed for MeOO**H**Me$^+$ in the same conditions. EtOO**H**$_2^+$, iPrOO**H**$_2^+$ and tButOO**H**$_2^+$ show very low barriers for step **R1c** (3.08, 1.21 and 0.12 kcal mol^{-1} respectively), and all three species are entirely (>99%) fragmented within ~1 μs. The final products of MeOO**H**$_2^+$ decomposition are protonated formaldehyde + H_2O (**P1**, 9.3%) and formaldehyde + H_3O^+ (**P2**, 7.7%). Water addition to the protonated carbonyl in **M2** is also possible for the MeOOH system, but it was not found to be an important reaction channel since the product is higher in energy and subsequent H_2 elimination (**R3b**) has a very high barrier. The major fragmentation products of all other alkyl-substituted ROO**H**$_2^+$ are a carboxonium ion + H_2O (**P3**). Complex **M6**'s constituting fragments can react with each other via nucleophilic substitution producing a protonated alcohol : aldehyde/ketone complex (**M7**), which can also undergo barrierless dissociation, yielding **P7**. However, this route was not observed to be competitive.

In contrast, protonation isomer RO**H**OH$^+$ is rather inert. Apart from isomerization into ROO**H**$_2^+$, only the three direct dissociation channels are available these: Heterolytic C-O bond cleavage yielding H_2O_2 and the corresponding carbocation R$^+$ (**R8**); Homolytic O-O bond cleavage yielding OH radical and a ROH$^{\bullet+}$ radical cation (**R9**); and a homolytic analogue of **R8**, yielding $H_2O_2^{\bullet+}$ radical cation and a carbon centered radical R$^\bullet$ (**R10**). Each of these channels was investigated for the other ROOH systems but, except for **R8** with tButO**H**OH$^+$, none were observed to contribute to decomposition within significant timescales, under the lower limit of excess energy scenario. For MeO**H**OH$^+$, the most favorable of these channels is **R9**, but the required energy is so high that the system would rather react through **R0a** to give MeOO**H**$_2^+$. **R8** dissociation energy decreases fast with increasing alkyl-substituent size, as the electron donating methyl groups stabilize the formed carbocation, and this step becomes the most favorable for the other RO**H**OH$^+$ systems. At 1.023 mbar, about 89.8% of tButO**H**OH$^+$ fragments into tert-butyl cation + H_2O_2 within 100 μs, while other RO**H**OH$^+$ remain unreacted.

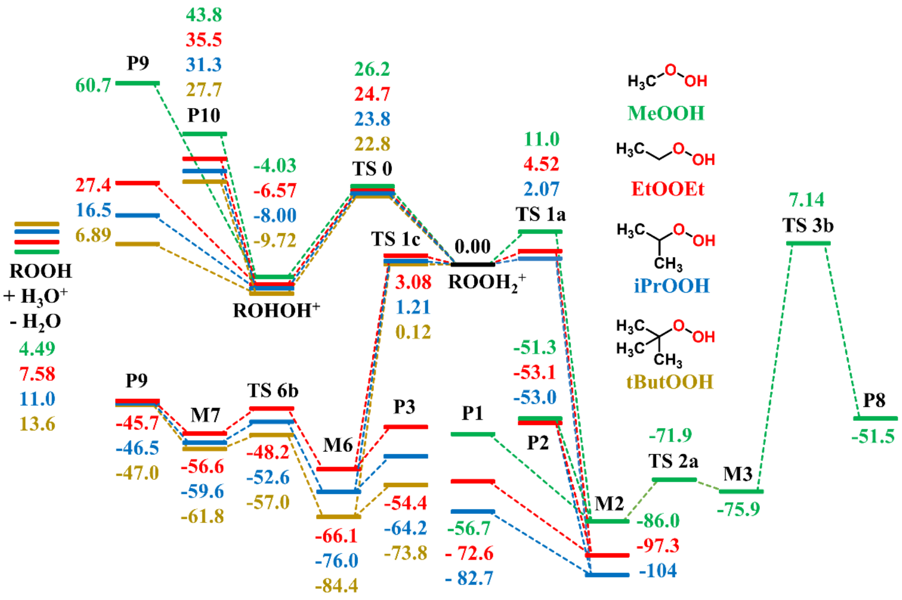

Figure S9. Potential energy surface calculated at the RHF-RCCSD(T)-F12a/VDZ-F12// ωB97XD/aug-cc-pVTZ level of theory, for decomposition of MeOOH (green), EtOOH (red), iPrOOH (blue) and tButOOH (yellow) following

protonation in the gas phase. Molecular structures for stationary points are shown in Scheme 3. Values given are relative zero-point corrected energies in kcal ~~.~~mol^{-1}.

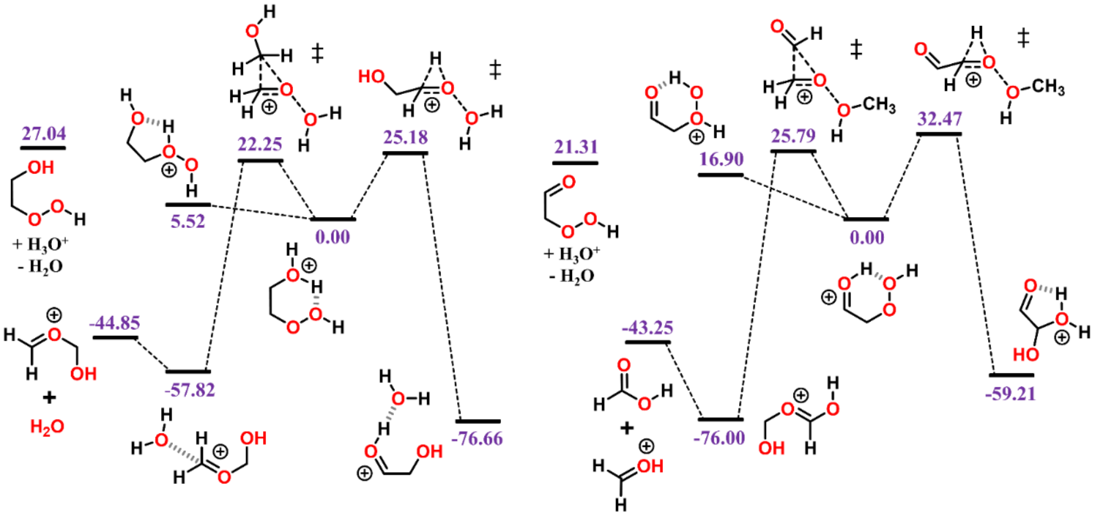

Figure S10. Potential energy surface calculated at the RHF-RCCSD(T)-F12a/VDZ-F12//ωB97XD/aug-cc-pVTZ level of theory for the initial steps in the decomposition of HOEtOOH (left) and O=EtOOH (right) following protonation in the gas phase. ~~Molecular structures carrying the double-dagger symbol ‡ are transition states.~~ Values given in purple are relative zero-point corrected energies in kcal ~~.~~mol^{-1}.

The calculations revealed that following protonation, HOEtOOH and O=EtOOH undergo little to no fragmentation within relevant time scales. Like with HOEtOOMe and O=EtOOMe, initial step **R1c** is favored over **R1a**. After 100 μs at 1.023 mbar, about 14.6% of HOEtOOH has fragmented into **P3**, while no significant amount of O=EtOOH has reacted. The underlying reason for the lower reactivities of these ROOH is the same as described previously for their ROOR' analogues: The intramolecular H-bond which stabilizes the protonated reactant is absent in the transition state of the initial steps **R1c** and **R1a**, resulting in higher reaction barriers (Figure S10). Furthermore, geometry optimizations indicate that the lowest energy conformation of the ROO**H**$_2^+$ isomer of these systems is not stable, undergoing barrierless H transfer to the alcohol/carbonyl group's oxygen, producing the more stable **H**$_2$OEtOOH$^+$ and **H**O=EtOOH$^+$ isomers. The RO**H**OH$^+$ isomers are possible but C-O or O-O scissions (**R8-10**) are unfavorable, and H-shift leading to the hydroxyl/carbonyl-protonated isomers (**R0c**) is very fast.

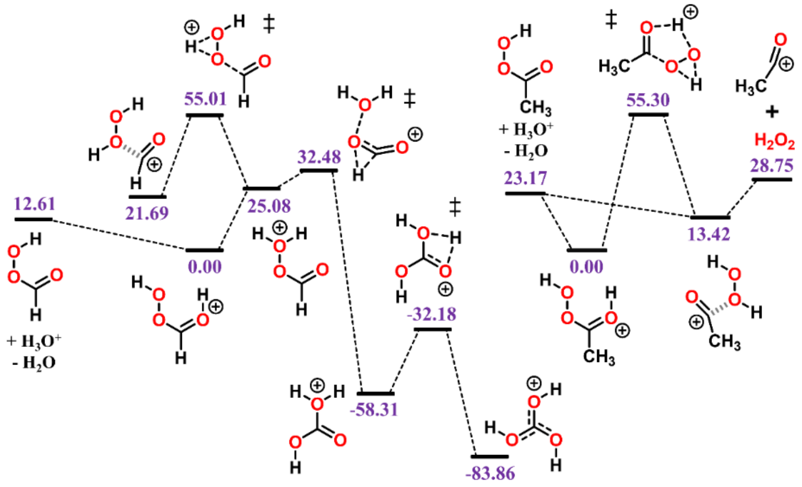

Figure S11. Potential energy surface calculated at the RHF-RCCSD(T)-F12a/VDZ-F12// ωB97XD/aug-cc-pVTZ level of theory for the reaction of peracetic acid (right) and performic acid (left) following protonation in the gas phase. ~~Molecular structures carrying the double-dagger symbol ‡ are transition states.~~ Values given in purple are relative zero-point corrected energies in kcal ~~·~~mol^{-1}.

Decomposition of the protonated peroxy acids follow a different mechanism than that shown in Scheme 3. Their potential energy surface is presented in Figure S11. Two protonation products were found for peracetic acid, the most stable being the carbonyl-oxygen protonated species (**H**AcOOH$^+$). Protonation of the peroxyl-oxygen atom adjacent to the acyl carbon occurs with concomitant C-O(OH) bond scission, leading to formation of an acylium ion (Ac$^+$) and H_2O_2 complex. The energy required for dissociation of this complex is higher than the excess energy released during protonation, and only ~0.6% of it fragments after 100 μs at 1.023 mbar. Interconversion between the Ac$^+$:H_2O_2 complex and **H**AcOOH$^+$ is possible but very unfavorable given the high reaction barrier involved (55.3 kcal ~~·~~mol^{-1}). Species AcOO**H₂**$^+$ is not stable, being rapidly converted into **H**AcOOH$^+$. Protonation of any oxygen atom in performic acid may result in a stable product, however the only exothermic channel produces the carbonyl-protonated isomer (**H**OCHOOH$^+$). No transition state was found for proton transfer from the carbonyl to the terminal peroxyl-oxygen, indicating this step should have a very low barrier. The produced isomer OCHOO**H₂**$^+$ has a decomposition reaction channel available that leads to the formation of protonated carbonic acid, however the overall barrier is too high (32.5 kcal ~~·~~mol^{-1}) and it doesn't happen at relevant time scales. Nevertheless, the elemental composition would be retained, and the mass spectrum signal would not be impacted. Similar to peracetic acid, protonation of the oxygen adjacent to the acyl carbon in performic acid would lead to formation of a formyl cation (HCO$^+$) and H_2O_2 complex.

S3.3 Cyclohexene oxidation products

A new reaction pathway (**R1d**) was found to be available for the ROOR and ROOH derived from ozonolysis of cyclohexene, depicted in Scheme S1. In it, instead of a 1,2-rearrangement of a H or an organyl group like in **R1a** or **R1c**, a more favorable 1,6 H$^+$-transfer occurs alongside the O-O bond scission. This reaction step is possible due to the presence of a carbonyl group situated at a further distance from the peroxide group and, for the ROOR system, it was observed to be dominant among decomposition steps involving rearrangement.

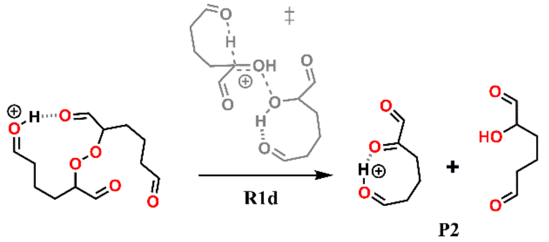

Figure S12. Initial decomposition step R1d, found for ROOR and ROOH derived from cyclohexene ozonolysis.

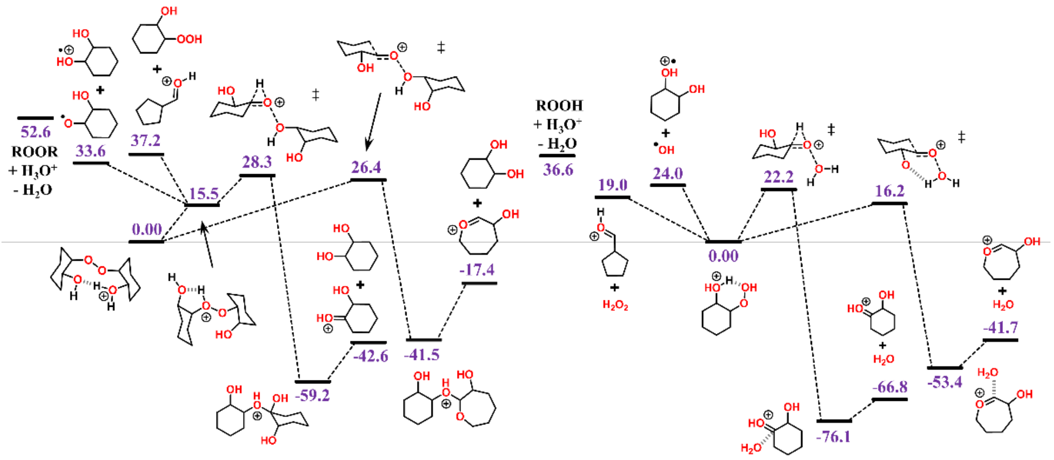

Figure S13. Potential energy surface calculated at the ωB97XD/aug-cc-pVTZ level of theory for reaction following protonation in the gas phase, for the ROOR (left) and ROOH (right) derived from cyclohexene oxidation by OH. ~~Molecular structures carrying the double-dagger symbol ‡ are transition states.~~ Values given in purple are relative zero-point corrected energies in kcal ~~.~~mol^{-1}.

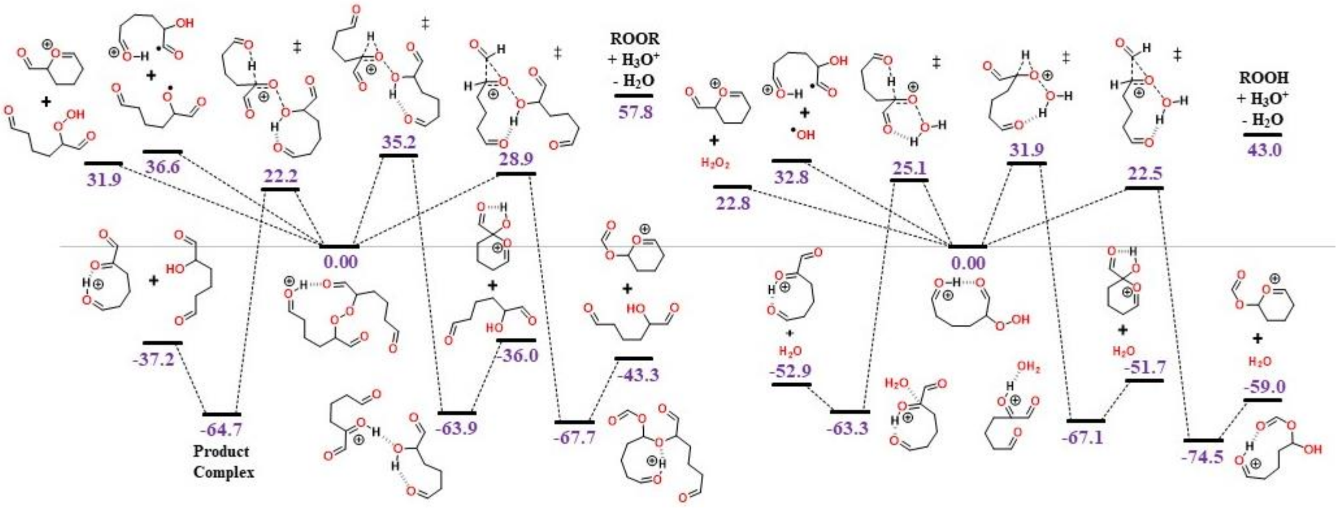

Figure S14. Potential energy surface calculated at the ωB97XD/aug-cc-pVTZ level of theory for reaction following protonation in the gas phase, for the ROOR (left) and ROOH (right) derived from cyclohexene oxidation by O_3. ~~Molecular structures carrying the double-dagger symbol ‡ are transition states.~~ Values given in purple are relative zero-point corrected energies in kcal ~~.~~mol^{-1}.

S3.4 High Energy Collisions.

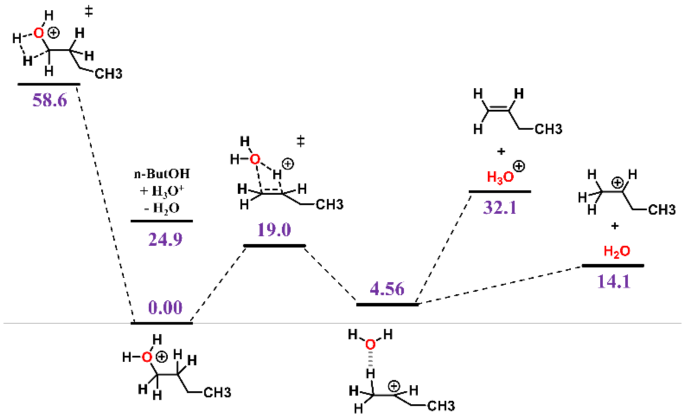

Figure S15. Potential energy surface calculated at the RHF-RCCSD(T)-F12a/VDZ-F12 // ωB97XD/aug-cc-pVTZ level of theory for reaction following protonation in the gas phase, for n-butanol. ~~Molecular structures carrying the double-dagger symbol ‡ are transition states.~~ Values given in purple are relative zero-point corrected energies in kcal ~~.~~mol^{-1}.

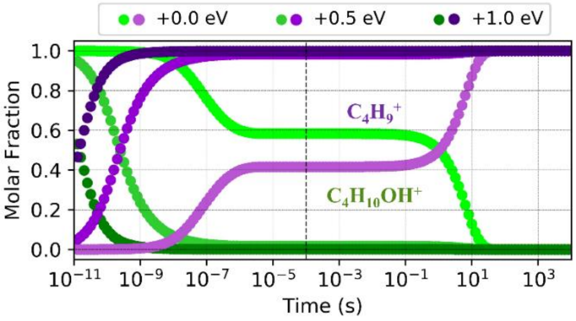

Figure S16. Reaction dynamics simulation results for n-butanol following protonation, under three excess energy scenarios. Graphs represent the time evolution profile of fragmentation, at 298.15 K and 1.013 mbar.

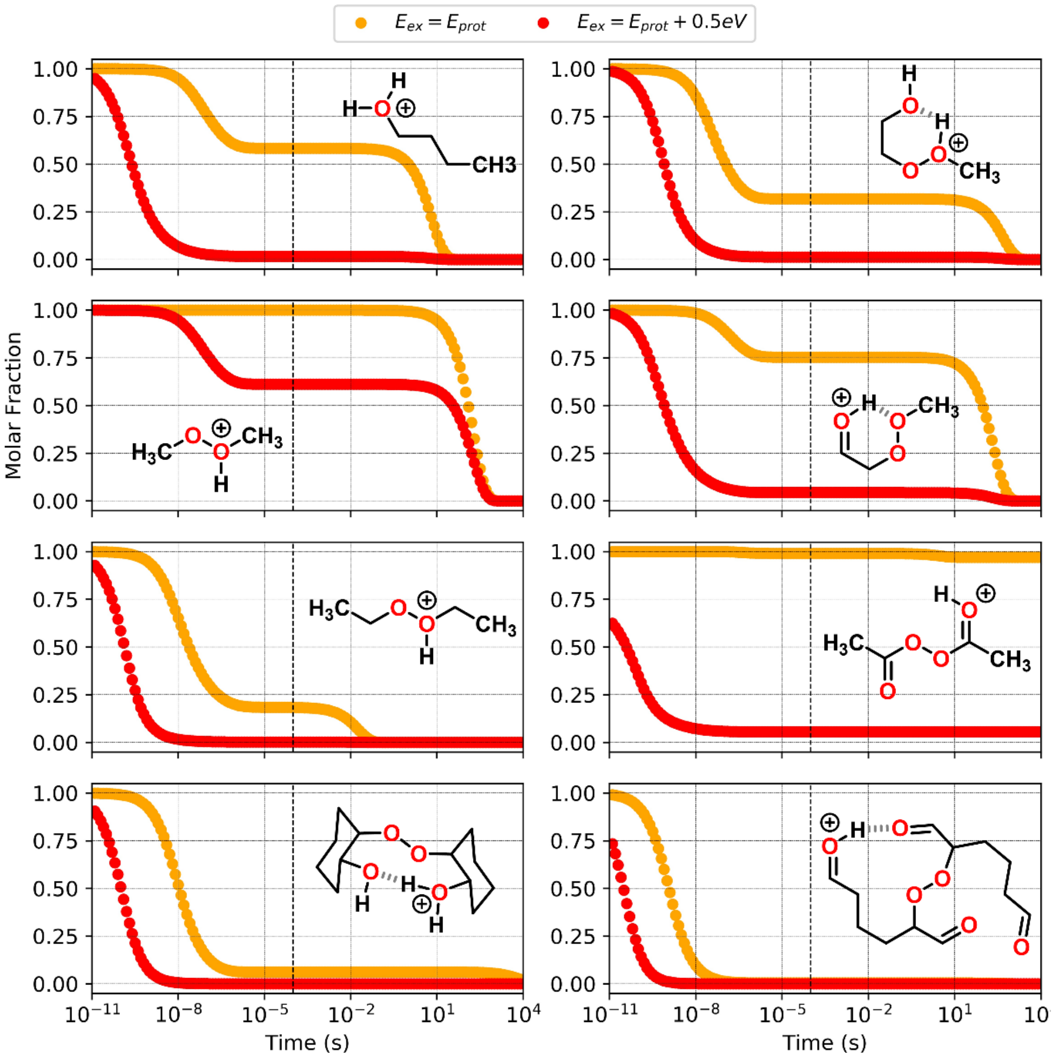

Figure S17. Reaction dynamics simulation results for n-butanol and the investigated ROOR systems, under two excess internal energy scenarios: Protonation energy only (orange) and protonation energy + 0.5 eV (red). Graphs represent the time evolution profile for reaction of initial protonated reactants, at 298.15 K and 1.013 mbar. 435

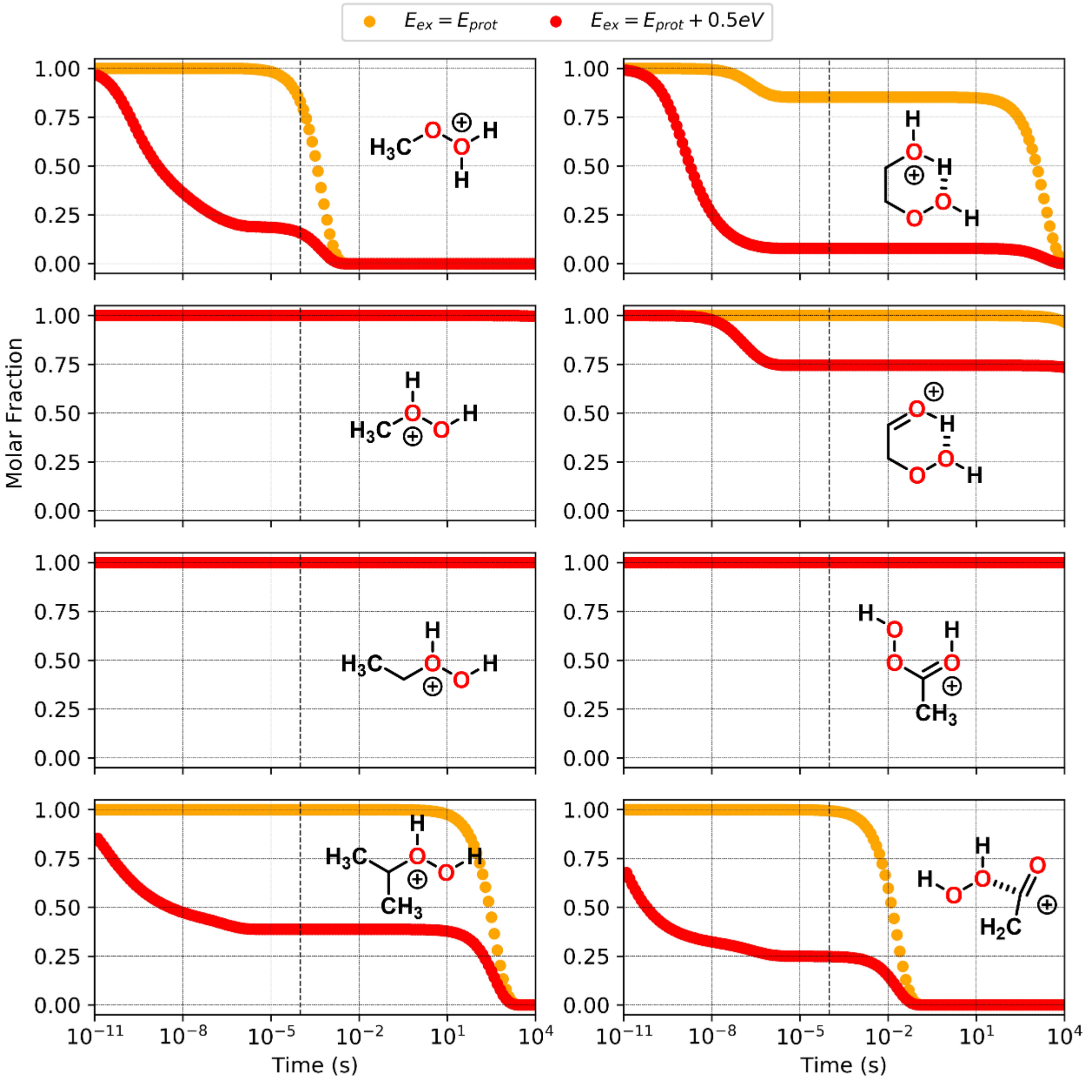

Figure S18. Reaction dynamics simulation results for the investigated ROOR systems, under two excess internal energy scenarios: Protonation energy only (orange) and protonation energy + 0.5 eV (red). Graphs represent the time evolution profile for reaction of initial protonated reactants, at 298.15 K and 1.013 mbar.

References

Cheung, P. S. Y. and Powles, J. G.: The properties of liquid nitrogen, Molecular Physics, 30, 921-949, 10.1080/00268977500102461, 1975.

Clayden, J., Warren, S. G., and Greeves, N.: Organic Chemistry, OUP Oxford, Oxford2012.

Dodda, L. S., Cabeza de Vaca, I., Tirado-Rives, J., and Jorgensen, W. L.: LigParGen web server: an automatic OPLS-AA parameter generator for organic ligands, Nucleic Acids Res, 45, W331-w336, 10.1093/nar/gkx312, 2017.

Eckart, C.: The Penetration of a Potential Barrier by Electrons, Physical Review, 35, 1303-1309, 10.1103/PhysRev.35.1303, 1930.

Garrec, J., Monari, A., Assfeld, X., Mir, L. M., and Tarek, M.: Lipid Peroxidation in Membranes: The Peroxyl Radical Does Not “Float”, The Journal of Physical Chemistry Letters, 5, 1653-1658, 10.1021/jz500502q, 2014.

Glowacki, D. R., Liang, C. H., Morley, C., Pilling, M. J., and Robertson, S. H.: MESMER: An Open-Source Master Equation Solver for Multi-Energy Well Reactions, J. Phys. Chem. A, 116, 9545-9560, 10.1021/jp3051033, 2012.

Hippler, H., Troe, J., and Wendelken, H. J.: Collisional deactivation of vibrationally highly excited polyatomic molecules. II. Direct observations for excited toluene, The Journal of Chemical Physics, 78, 6709-6717, 10.1063/1.444670, 1983.

Jorgensen, W. L. and Tirado-Rives, J.: Potential energy functions for atomic-level simulations of water and organic and biomolecular systems, Proceedings of the National Academy of Sciences of the United States of America, 102, 6665, 10.1073/pnas.0408037102, 2005.

Jorgensen, W. L., Maxwell, D. S., and Tirado-Rives, J.: Development and Testing of the OPLS All-Atom Force Field on Conformational Energetics and Properties of Organic Liquids, J. Am. Chem. Soc., 118, 11225-11236, 10.1021/ja9621760, 1996.

Kaminski, G. A., Friesner, R. A., Tirado-Rives, J., and Jorgensen, W. L.: Evaluation and Reparametrization of the OPLS-AA Force Field for Proteins via Comparison with Accurate Quantum Chemical Calculations on Peptides, The Journal of Physical Chemistry B, 105, 6474-6487, 10.1021/jp003919d, 2001.

Lee, M.-T., Orlando, F., Khabiri, M., Roeselová, M., Brown, M. A., and Ammann, M.: The opposing effect of butanol and butyric acid on the abundance of bromide and iodide at the aqueous solution–air interface, Phys. Chem. Chem. Phys., 21, 8418-8427, 10.1039/C8CP07448H, 2019.

Lee, S. and Kim, J.: Molecular Dynamics Simulation Study of Transport Properties of Diatomic Gases, Bulletin of the Korean Chemical Society, 35, 3527-3531, 10.5012/bkcs.2014.35.12.3527, 2014.

Michael, J. V., Su, M. C., Sutherland, J. W., Carroll, J. J., and Wagner, A. F.: Rate Constants For H + O2 + M → HO2 + M in Seven Bath Gases, The Journal of Physical Chemistry A, 106, 5297-5313, 10.1021/jp020229w, 2002.

Miller, J. A. and Klippenstein, S. J.: Master Equation Methods in Gas Phase Chemical Kinetics, The Journal of Physical Chemistry A, 110, 10528-10544, 10.1021/jp062693x, 2006.

Pilling, M. J. and Robertson, S. H.: Master Equation Models for Chemical Reactions of Importance in Combustion, Annual Review of Physical Chemistry, 54, 245-275, 10.1146/annurev.physchem.54.011002.103822, 2003.

Plimpton, S.: Fast Parallel Algorithms for Short-Range Molecular Dynamics, Journal of Computational Physics, 117, 1-19, https://doi.org/10.1006/jcph.1995.1039, 1995.

Schalley, C. A., Dieterle, M., Schroder, D., Schwarz, H., and Uggerud, E.: On the cleavage of the peroxide O-O bond in methyl hydroperoxide and dimethyl peroxide upon protonation, Int. J. Mass Spectrom. Ion Process., 163, 101-119, 10.1016/s0168-1176(97)00001-3, 1997.

Senosiain, J. P., Klippenstein, S. J., and Miller, J. A.: Pathways and Rate Coefficients for the Decomposition of Vinoxy and Acetyl Radicals, The Journal of Physical Chemistry A, 110, 5772-5781, 10.1021/jp054934r, 2006.

Shi, H. C., Wang, Y. L., and Hua, R. M.: Acid-catalyzed carboxylic acid esterification and ester hydrolysis mechanism: acylium ion as a sharing active intermediate via a spontaneous trimolecular reaction based on density functional theory calculation and supported by electrospray ionization-mass spectrometry, Phys. Chem. Chem. Phys., 17, 30279-30291, 10.1039/c5cp02914g, 2015.

Su, T. and Chesnavich, W. J.: Parametrization of the ion-polar molecule collision rate-constant by trajectory calculations, J. Chem. Phys., 76, 5183-5185, 10.1063/1.442828, 1982.

Tardy, D. C. and Rabinovitch, B. S.: Intermolecular vibrational energy transfer in thermal unimolecular systems, Chemical Reviews, 77, 369-408, 10.1021/cr60307a004, 1977.

Wang, L., Ceriotti, M., and Markland, T. E.: Quantum kinetic energy and isotope fractionation in aqueous ionic solutions, Phys. Chem. Chem. Phys., 22, 10490-10499, 10.1039/C9CP06483D, 2020.